Dissertation
submitted to the
Combined Faculties for the Natural Sciences and for Mathematics
of the Ruperto-Carola University of Heidelberg, Germany
for the degree of
Doctor of Natural Sciences

presented by Diplom-Physiker Arnold Giske
born in Almaty, Kasachstan
oral examination: 07. November 2007

CryoSTED microscopy
A new spectroscopic approach for improving the resolution of STED microscopy using low temperature

Referees: Prof. Dr. Stefan Hell
Prof. Dr. Christoph Cremer

Abstract

This work presents a new approach for the further improving of the resolution in the sub-diffraction fluorescence STED microscopy. The reduction of the sample temperature down to 76K eliminates the disadvantages of anti-Stokes fluorescence excitation and allows the use of wavelengths with larger STED efficiencies. On the studied dyes, this approach enhances the resolving power by a factor of 1.6 compared to room temperature and suggests further technical improvements for such resolution increase. Besides resolution, the present work solves the issue of the high triplet population in fluorescence imaging at liquid nitrogen temperature. A technique for the triplet depopulation has been developed. It provides a manifold brightness increase in the fluorescence imaging at low temperatures. The utilization of the low temperature also increases the photo-stability of the fluorescent markers. The combination of a complete triplet depopulation and higher fatigue resistance allows an enhanced signal to noise ratio in STED and fluorescence microscopy in general.

Zusammenfassung

Dieser Arbeit präsentiert einen neuen spektroskopischen Ansatz, um die Auflösungserhöhung in der hochauflösenden STED Fluoreszenzmikroskopie weiter zu verbessern. Die Reduzierung der Temperatur bis zu 76K erlaubt den Einsatz von STED Wellenlängen mit höheren Wirkungsquerschnitten für die stimulierte Emission. Es wird gezeigt, dass deren Einsatz zu einer relativen Auflösungserhöhung von 1,6 im Vergleich zu den bei Raumtemperatur einsetzbaren Wellenlängen führt. Allerdings bedingt das Arbeiten bei tiefen Temperaturen eine deutlich höhere Tripletbevölkerung und somit eine Verschlechterung des Signal-zu-Rausch Verhältnisses in der fluoreszenzbasierten Bildgebung allgemein. Dies kann durch ein in dieser Arbeit entwickeltes Verfahren zur Entvölkerung des Tripletzustands vermieden werden. Zudem ist die Photozerstörung der fluoreszenten Moleküle ebenfalls stark reduziert bei tiefen Temperaturen. Sowohl die lichtgetriebene Tripletentvölkerung als auch die hohe Photostabilität bei tiefen Temperaturen verbessern das Signal-zu-Rausch Verhältnis in der STED und Fluoreszenzmikroskopie.

Contents

Chapter 1

Introduction

Motivation

In microscopy, the term resolution refers to the minimum distance between two point-like objects, which can still be told apart. Imaging studies of tiny structures necessitates the use of tools with the appropriate resolving power. In case of the life sciences, especially disciplines like biology and medicine, optical far-field microscopy has afforded great discoveries and allowed very useful techniques over the past few centuries. Optical far-field microscopy provides the ability to look inside cells, which are elemental units of living creatures. An introduction of fluorescence immunolabeling has leveraged far-field microscopy to most popular imaging technique in the living science domain.

Typical sizes of cellular structures appear at different sizes ranging from 20nm (ribosome and microtubule) to 10μm (nucleus). Some proteins, the driving units of molecular biochemistry, are very often even smaller than 10nm. The resolving power of a far-field microscope is limited due to diffraction of light to nearly 200nm. Since some details in cells remain unveiled due to the diffraction barrier, the scientific community continues to develop new approaches to overcome the diffraction limit by exploiting different effects in a smart way. One of these techniques is STED microscopy - an improved version of far-field fluorescence microscopy.

This work uses a spectroscopic approach to study the key factor of STED microscopy, stimulated emission cross section, and improve the resolving power of current fluorescence STED microscopes. The studies are carried out at liquid nitrogen temperatures to eliminate the contribution of anti-Stokes excitation. The goal is to find optimal conditions for maximum STED efficiency and highlight the necessary ingredients for maximum resolution. This work lays the foundation for developing an optical fluorescence microscope with resolving power below 10nm.

1.1 Optical microscopy

Optical far-field microscopy began with the publication of Robert Hook [1], where he presented detailed copper plate engravings of small insects and plant cells observed with *"'various lenses"'*. Soon a growing community of natural scientists adopted optical microscopy due to its ease of use and its magnificent resolution ability for those times. In 1873, almost two centuries after R. Hook, Ernst Abbe deduced the formula for maximum resolution Δr of an optical far-field microscope:

$$\Delta r = \frac{0.61\lambda}{\mathrm{NA}} \tag{1.1}$$

where λ is the wavelength of light and NA is the numerical aperture of the utilized objective lens [2]. The term $\mathrm{NA} = n\sin(\alpha)$ describes the maximal angle α of incident light which contributes to the focused light spot (so called point spread function (PSF)) and to the detection PSF.

Since the wavelength spectrum of visible light ranges from 400nm up to 750nm and the commonly utilized value of NA is 1.4, the resolution of an optical far-field light microscope is limited to $\sim$200nm. Many attempts have been undertaken to circumvent the diffraction limit by applying shorter wavelengths (electron [3] and x-ray microscopy [4, 5]) or even discarding the far-field concept and using evanescent wave fields (total internal reflection (TIRF) [6] and scanning near-field optical microscopy (SNOM) [7]). These techniques provide great resolution ability (down to several nanometers in the case of electron microscopy), often combined with destructive specimen preparation. In electron and X-Ray microscopy, the energy of applied photon or electron beams is very high and the specimen absorb these, thereby getting damaged. Therefore only observation of thin slices less then 100nm thickness is possible. To this end the cells are shock-frozen and cut into sections of desired thickness. On the other hand, near-field techniques provide great resolution of approximately 50nm (SNOM). They are however highly surface susceptible with an inability to look below the surface inside the cells. The observation of 3D structure with those techniques is then only possible with the effort of mechanical cut sectioning and subsequent imaging of each section.

In contrast to these techniques, far-field optical microscopy provides ease of use. Moreover there are almost no restrictions on the specimen because visible light goes through biological tissue without being absorbed or destroying the sample. However, the major force behind its dominance in the life sciences is the invention of immunolabeling with fluorescent markers [8] and the subsequent discovery of "'native"' expression of fluorescent proteins inside cells [9]. The greatest advantage here is the high selectivity of observable regions. By using a specific binding antibody, nearly every region of interest inside a cell can be "'colored"' with fluorescent markers. In the case of fluorescent proteins, an additional DNA sequence, a plasmid, allows cells to express

a target protein, tagged with a fluorescent protein. Fluorescent markers, molecules which can emit light, provide very large signal to noise ratio due to the Stokes shift of the emission wavelength with respect to the excitation wavelength [10]. The combination of these techniques with a confocal microscope [11] provides a superior tool with diffraction limited resolution of 200nm and high selectivity of observable structures. Since a lot of details inside the cell are below the diffraction limit, increasing the resolving power of optical fluorescence microscopes is a hot topic.

1.2 Super-resolution in fluorescence microscopy

In the past two decades, several interesting ideas to break the diffraction limit in fluorescence microscopy have been proposed. The most promising concepts for resolution enhancement are the RESOLFT [12] and the PALM [13, 14] concepts.

The term RESOLFT is an abbreviation for **RE**versible **S**aturable **O**ptica**L** (**F**luorescent) **T**ransition. We need two ingredients for RESOLFT - a light-driven, saturable and reversible transition between two states, A and B, as well as an intensity distribution with a well-defined zero, and an optimal slope around this zero. The states A and B must be distinguishable by at least one measurable property. In optical microscopy, fluorescence emission is very often used as the probe property. But, in principle, the RESOL(F)T concept is not necessarily bound to that. To obtain images from a specimen, all molecules are prepared to be in the state A. A modified intensity distribution of de-excitation light with a well defined zeros then is applied to specimen. This light drains the molecules from state A to state B everywhere except at the position(s) with zero intensity. Afterwards, the specimen is probed for state A. Now only those molecules in close vicinity of the zero intensity position will be detected. After the acquisition of information for this pixel, the molecules need to be reversed into state A completely for further cycles. The specimen is scanned pixel-wise by shifting the zero intensity position over the sample. The resolution of the image is given by the lateral width of distribution of state A molecules around the zero - an effective RESOLFT PSF. The molecules undergo the cycle $A \rightarrow B$ many times and contribute to the image construction only when they are in close vicinity of the de-excitation intensity zero. The resolving power within this concept depends on the saturation level of the $A \rightarrow B$ transition and the number of cycles before the molecules are photo-destructed. To date, a large variety of optical transitions have been utilized in optical microscopy with sub-diffraction resolving powers beyond the diffraction barrier down to 20nm [15–19].

The term PALM stands for **P**hoto**A**ctivated **L**ocalization **M**icroscopy and the idea takes advantage of the single, photo-switchable molecule events and the very high localization ability of those. The photo-switchable molecules are gently activated in such a manner so that the density of fluorescing molecules is sufficiently low, thereby

ensuring that only single events are counted. Every single fluorescence burst can be localized with very high precision by a centroid analysis [20], the precision ability is given by the size of activation light spot divided by square root of the photon number within this burst. The sub-diffraction image is constructed by mapping the positions of the single bursts. The resolving power is limited by the number of photons which come from one particular molecule. Recent experimental work has shown an increase of resolution down to 10nm with acquisition times of around one day [13] and 20nm with acquisition times of several minutes [21] in the lateral direction.

1.3 Concept of stimulated emission depletion

The first and most developed concept among the RESOLFT family is the idea to use stimulated emission as the $A \rightarrow B$ transition for resolution enhancement [22, 23]. In this case, state A represents the fluorescent first excited state S_1 of molecules, and B the non-fluorescent ground state S_0. Figure 1.1 shows a simple energy diagram of

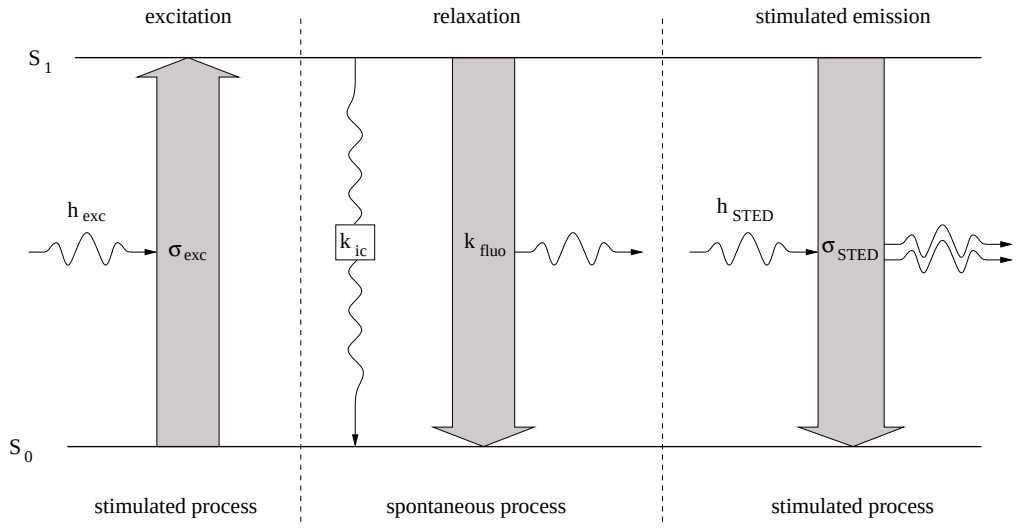

Figure 1.1: Simple two state model for stimulated emission.

the parameters involved. First, the molecules are excited to the first electronic state S_1 with a certain rate $\sigma_{exc}h_{exc}$, given by the product of the excitation cross section σ_{exc} and the excitation photon flux h_{exc}. The reverse transition can occur in two possible ways: (1) they relax spontaneously to the ground state S_0 by emitting a photon with the fluorescence rate k_{fluo} or radiationless by the internal conversion k_{ic}, or (2) the incoming photon flux h_{STED} can stimulate the transition with the rate, given by the product of

stimulated emission cross section and the triggering photon flux $\sigma_{\mathrm{STED}} h_{\mathrm{STED}}$. In case of high STED efficiency ($\sigma_{\mathrm{STED}} h_{\mathrm{STED}} \gg k_{ic} + k_{fluo}$) the spontaneous pathways can be neglected.

The population of the electronic states $\mathrm{S}_1, \mathrm{S}_0$ is then given by the rate equation:

$$\begin{aligned} \frac{d}{dt}\mathrm{S}_1(t) &= -\sigma_{\mathrm{STED}} h_{\mathrm{STED}} \mathrm{S}_1(t) + \sigma_{\mathrm{exc}} h_{\mathrm{exc}} \mathrm{S}_0(t) \\ \frac{d}{dt}\mathrm{S}_0(t) &= -\sigma_{\mathrm{exc}} h_{\mathrm{exc}} \mathrm{S}_0(t) + \sigma_{\mathrm{STED}} h_{\mathrm{STED}} \mathrm{S}_1(t) \end{aligned}$$

In general, two cases can be differentiated. In the case of simultaneous excitation and stimulated emission, both rates compete against one another and the solution for steady state condition (temporal derivatives equal to zero) is given by:

$$\mathrm{S}_1(h_{\mathrm{STED}}) = \frac{\sigma_{exc} h_{exc}}{\sigma_{exc} h_{exc} + \sigma_{\mathrm{STED}} h_{\mathrm{STED}}} \tag{1.2}$$

This case occurs for continuous wave (CW) excitation and de-excitation. If the excitation and stimulated emissions are driven by pulsed lasers, and are thus temporally separable, the de-excitation pulse is optimally tuned to come subsequent to the excitation [24]. In this case, the excitation cross section can be neglected and the solution for the S_1 population is given by

$$\mathrm{S}_1(h_{\mathrm{STED}}) = \exp(-\sigma_{\mathrm{STED}} h_{\mathrm{STED}}) \tag{1.3}$$

The expressions 1.2 and 1.3 are plotted in figure 1.2. The development of depletion is different for the initial intensity values because in the case of CW solution (red curve) the excitation cross section competes against the stimulated emission cross section. However, both characteristics show the depletion of the fluorescent S_1 state population down to zero.

By using the relation $h_{\mathrm{STED}} \sim I$ the expression 1.3 can be rewritten as a function of the STED laser intensity I:

$$\begin{aligned} \mathrm{S}_1 &= \exp(-\tilde{\sigma}_{\mathrm{STED}}\, I) \\ &\doteq \exp\left(-\frac{I}{I_{\mathrm{SAT}}}\right) \end{aligned} \tag{1.4}$$

The saturation intensity I_{SAT} is an experimentally accessible parameter from the saturation characteristic, where the S_1 population is reduced to $1/e$ of its initial value. In combination with the applied intensity I, we can define a saturation ratio $\xi = I/I_{\mathrm{SAT}}$.

Another ingredient for stimulated emission depletion microscopy is a well defined de-excitation intensity pattern with distinguishable zero intensity positions. Figure 1.3(a) shows the appropriate intensity distributions. While the excitation light illu-

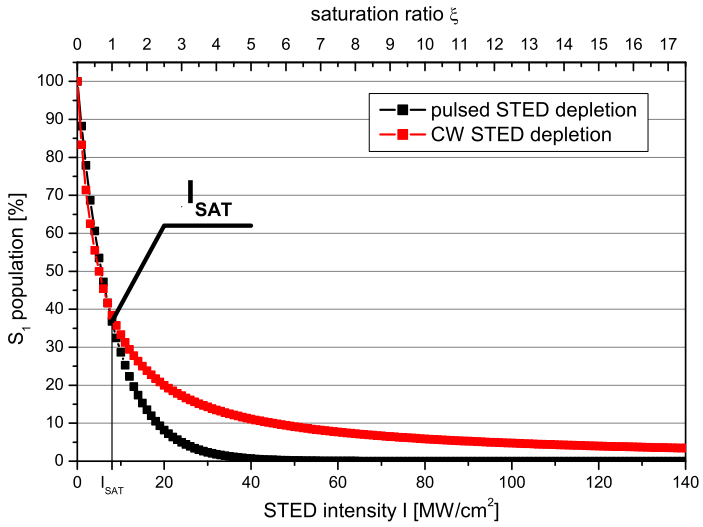

Figure 1.2: Depletion of S_1 population, and thus remaining fluorescence emission, due to stimulated emission with STED intensity I for CW (red squares) and pulsed (black squares) excitation and de-excitation.

minates the specimen with constant intensity (left lower image), the STED intensity distribution is modified with the expression $\sin^2(x) + \sin^2(y)$ (left upper image). This modified intensity pattern can be achieved by the interference of several beams with appropriate phase and intensity modulations [25], and provides a grid of spatially distinguishable STED intensity zeros. Since the STED intensity distribution applies with the saturation characteristic from the expression 1.4 (right upper image) to the fluorescence, the resulting remaining fluorescence distribution show bright spots in the close vicinity to the STED intensity zeros (right lower image). The specimen can be scanned with the resulting effective PSF, the resolution enhancement is provided by the constriction of the spatial fluorescence distribution around the STED intensity zero with a high saturation ratio ξ. Figure 1.3(b) shows the shape of a single effective fluorescence spot for different saturation ratios ξ in lateral direction.

Analyzing the intensity shape characteristic close to the zero and the saturation ratio ξ, one can deduce the expression for the resolving ability of the described microscope [26]:

$$\Delta(x,y) = \frac{\lambda}{\pi}\arcsin\left(\xi^{-1/2}\right) \tag{1.5}$$

$$\sim \frac{\lambda}{\pi \mathrm{NA}\sqrt{\xi}} \tag{1.6}$$

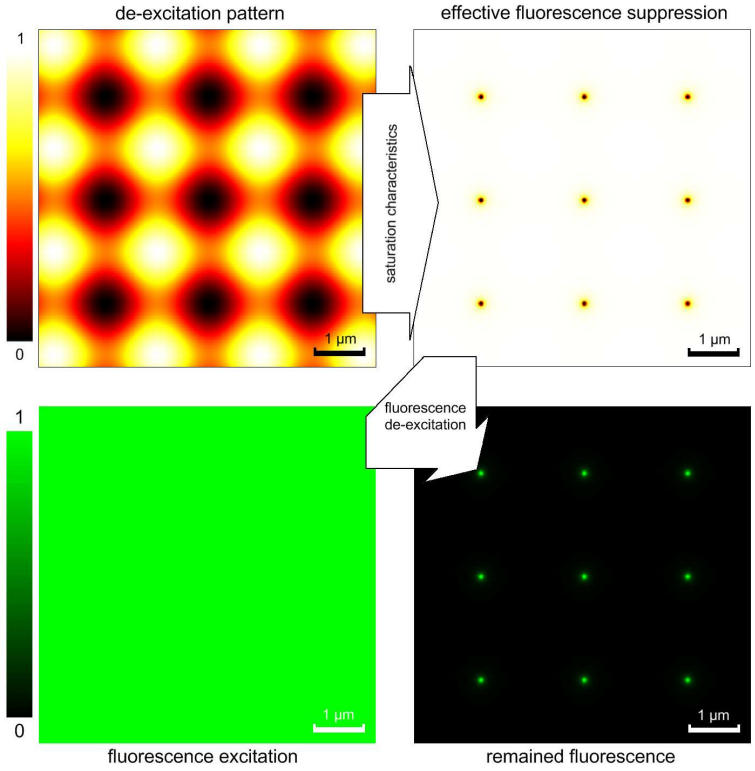

(a) Construction of the super-resolved effective PSF by combining a modulated STED intensity (left upper image), saturated with $\xi = 50$ (right upper image) with the homogeneous fluorescence excitation (left lower image). The resulting remaining fluorescence distribution (right lower image) provides an effective PSF with sub-diffraction size.

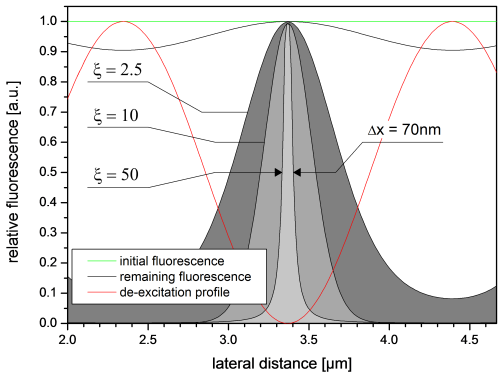

(b) Line profile through the effective PSF for different saturation ratios ξ.

Figure 1.3: Sub-diffraction resolution enhancement within the concept of STED microscopy.

In the special case of a confocal microscope, the excitation illumination is provided by a single, diffraction limited laser spot. The resolution is given by a convolution of the excitation PSF with a detection PSF [27] and is slightly better than the Abbe rule [2]:

$$\Delta r = \frac{0.5\lambda}{\mathrm{NA}} \tag{1.7}$$

in the lateral direction. A resolution increase is then provided by a saturable stimulated emission transition from the fluorescent first excited state into the dark ground state in the same manner as described in figure 1.3. The fluorescence is quenched by an appropriately modified intensity distribution, generated by the application of special phase masks, which produce an asymptotically parabolic intensity distribution around the zero [25]. The development of the effective PSF looks nearly the same, as shown in figure 1.3(b). The resolution enhancement can be expressed as followed [28]:

$$\Delta r = \frac{0.61\lambda}{\mathrm{NA}\sqrt{1+\xi}} \tag{1.8}$$

with ξ intensity saturation ratio I/I_{SAT}.

1.4 Advances in present day STED microscopy

STED microscopy, as an improvement of far-field fluorescence microscopy, was first suggested in 1994 and the first experimental demonstration took place in 1999 [22, 23]. Subsequently STED microscopy was continuously improved. First, phase retardation masks were introduced to generated optimal de-excitation intensity distributions for 2D and 3D resolution. This led to a resolution enhancement of upto 97nm in the axial and 104nm in the lateral dimensions while utilizing a 3D phase mask [29]. The best axial resolution of 33nm was reached some time later by combining a 4Pi microscope with the STED concept [30]. Introduction of optimized phase masks, which provide optimal slope around the STED intensity zero for lateral resolution [31], has improved the resolution to 16nm on single molecules [32] and ∼60nm in biological specimen [33].

Tackling such problems, resolution down to macromolecular scale have been demonstrated recently. Realizing, that the most efficient pathway for the photo-bleaching occurs via the dark state of fluorescent markers, a simple idea of complete triplet relaxation between the excitation pulses was implemented in the D-Rex STED microscopy. This technique has provided lateral resolutions of 20nm in biological samples recently [19]. By eliminating the triplet channel contribution to photo-bleaching by using reduced excitation frequency simply allows the use of higher de-excitation intensities in biological specimen and leads to 10 times higher saturation ratio than

before.

The resolution in STED microscopy is mainly limited by two key factors - the maximum saturation ratio ξ and the photo-stability of the fluorescent dye molecules during cycles from $S_1 \rightarrow S_0$ and reverse. Therefore the main task for improving STED microscopy in terms of increasing the resolution lies in improving these key factors.

1.5 Resolution increase by optimizing the STED cross section

The use of D-Rex STED microscopy scheme [19] has dramatically reduced the bleaching probability due to elimination of the triplet population, and has increased the applicable laser intensities and thereby the saturation ratio $\xi = I/I_{\mathrm{SAT}}$. Since the saturation intensity I_{SAT} is reciprocal to the cross section of the stimulated emission σ_{STED}, the saturation ratio ξ can be increased by optimizing σ_{STED}. On the basic of work on dye lasers from the 70's and 80's, it is known that the cross section for the stimulated emission is proportional to the spectrum of spontaneous fluorescence emission [34], [35]. Thus the best stimulated emission cross section, and thereby the maximum saturation ratio ξ is obtainable for those STED wavelengths which are the same as the values of the maximum fluorescence emission spectrum of the used fluorophore.

This is exemplified in figure 1.4. The present day microscopes utilize STED wavelengths within the far-red edge of the emission spectrum of a fluorophore. This provides the relative STED cross sections below 12% in [33] or 18% in [19] in respect to the value at maximum of the spontaneous emission. The reason behind the choice of such red-shifted STED wavelengths is the additional fluorescence signal, which is caused by the $S_0 \rightarrow S_1$ absorption induced by the STED light. This direct fluorescence excitation, so called anti-Stokes excitation, competes with the stimulated emission and thereby reduces the saturation ratio ξ.

The utilization of shorter STED wavelengths promises a higher stimulated emission cross section, as shown in figure 1.4 for the fluorescent marker Atto532. In this case, the use of 553nm as STED wavelength promises an increase of saturation ratio ξ by a factor of 5.8 with respect to $\lambda_{\mathrm{STED}} = 605\mathrm{nm}$. For the utilization of such STED wavelengths, a strong suppression of the anti-Stokes excitation is necessary.

The origin of the anti-Stokes excitation is believed to be the Boltzmann distributed occupation of high excited vibrational states within the electronic ground state S_0. For these states the energy gap to first electronic excited state S_1 is reduced, thus the transition $S_0 \rightarrow S_1$ by absorption of a red-shifted STED photon becomes probable. The occupation number of a particular vibrational state with the energy E_{vib} is given by

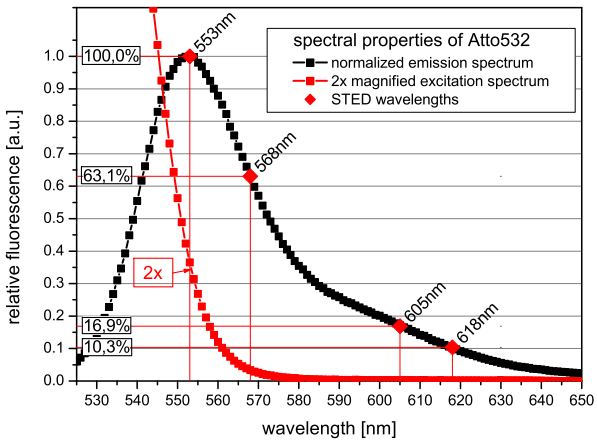

Figure 1.4: A survey over the spectral properties of Atto532. The emission (black squares) and excitation (2× magnified, red squares) spectra are compared with the desirable STED wavelengths and their cross sections (red rhombus).

Boltzmann distribution:

$$f\left(E,T\right)=\exp\left(-\frac{E_{vib}}{k_BT}\right)$$

where k_B is the Boltzmann constant and T is the temperature. According to this expression, a linear reduction of the temperature would cool down the occupation distribution exponentially, and thereby reduce the anti-Stokes excitation.

This work introduces the use of liquid nitrogen temperature in STED microscopy for cooling down the anti-Stokes excitation, and thereby allowing the utilization of STED wavelengths with larger stimulated emission cross sections a what is available to date. The theoretical considerations on stimulated emission cross section as well as experimental findings in dye laser research promise an enhancement in the resolving power of factor 2.2 for the in figure 1.4 shown Atto532.

Also the heighten photo-bleaching probability within the STED concept due to more often cycling between the S_0 and S_1 states off-side the intensity zeros, is expected to be strongly reduced at low temperatures. The most prominent pathway for the photo-bleaching is referred to the probability of a chemical reaction of the excited fluorescent molecule with a diffusing oxidizing agents, such as oxygen [36]. The chemical reaction rate k depends exponentially on the temperature T:

$$k=A\exp\left(-\frac{E_A}{k_BT}\right) \tag{1.9}$$

where A is a pre-exponential factor, E_A is the activation energy for a chemical reaction

and k_B is the Boltzmann constant. This relation is known as the Arrhenius law. So, a reduction of T from the room temperature to the liquid nitrogen temperature reduces the rate of a chemical reaction by a factor of $\sim$44. The diffusion constant is also suppressed by a similar expression as equation 1.9, where the constant E_A^* is declared as the activation energy of duffusion.

The CryoSTED microscopy improves the key factors of the STED concept - the STED efficiency and the photo-bleaching resistivity.

Chapter 2

The CryoSTED setup

2.1 Liquid nitrogen flow-through cryostat

The studies at low temperature necessitate the use of a cryostat. For this work, a commercially available microscopy cryostat, ST-500-LN from Janis Research Company, USA is used. It uses a flow-through technique where a cold gas is pumped with a membrane pump (ILMVAC GmbH, Germany) at a constant flux, from a dewar through a spiral tube inside a cooling finger, and thereby reduces the sample temperature by heat exchange. Liquid nitrogen is used as the cooling gas, the lowest temperature which can be reached is 74K due to reduction of the vapor pressure above the liquid nitrogen surface. Any temperature between 74K and 350K can be set by an additional 50W electrical resistance ring heater, the temperature is stabilized with a PID closed loop regulator.

Figure 2.1 shows a schematic of the cryostat used. The liquid nitrogen lowers the temperature of the cooling finger down to the desired temperature and is stabilized by the 50W electrical resistance ring heater. A sample holder, made out of brass for optimal thermal conductivity, is screwed into the cooling finger. The sample, a fluorescent specimen between two round cover glasses, is attached to the sample holder with glycerin to assure good thermal contact. The quality of the thermal contact is tested in several runs by comparing the display of temperature controller with the read-out of an extra thermocouple installed inside the sample. The measured difference between the temperature of the cooling finger (see schematic in fig. 2.1) and the temperature inside the sample is below 3K at 76K. The stated temperature for all further measurements is the displayed value on the temperature controller.

The use of such low temperatures T(LN_2)$= -196°$C below the freezing point of water necessitates an effective protection from water condensation, which would otherwise build an ice shelf around the sample within a very short time. Thus the sample holder

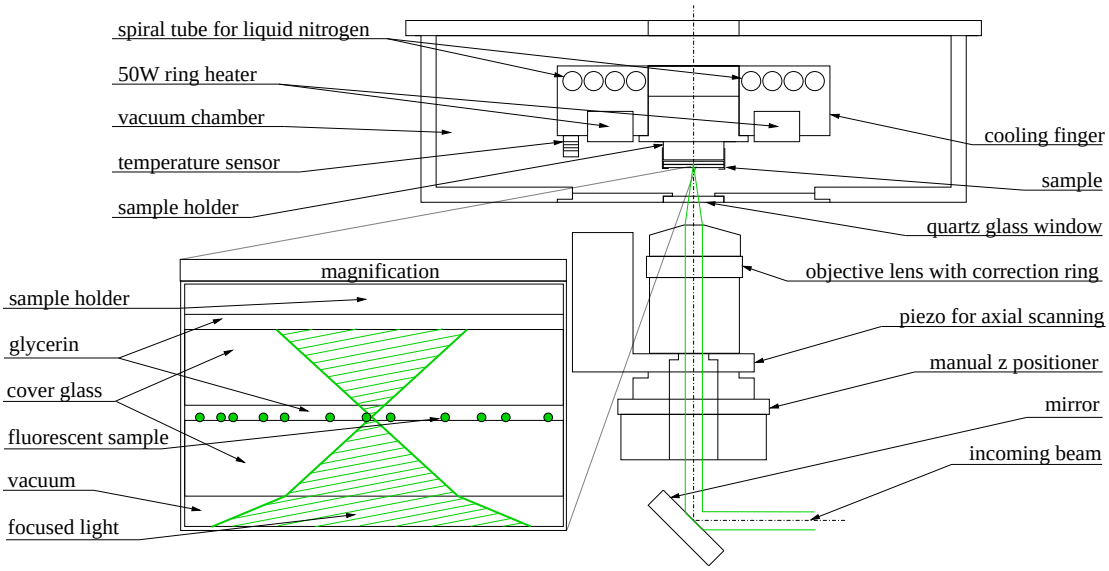

Figure 2.1: A technical schematic of the cryostat, assembled with an air objective lens.

is placed inside a vacuum chamber, which is evacuated by a turbo molecular pump (Turbo Cube from Pfeiffer, Germany) to a pressure below 1×10^{-5} mbar.

For the optical beam transmission, a quartz glass window with the flatness of $\lambda/5$ and 500 μm thickness is installed. The cryostat is mounted on a stage which can be tilted with respect to the optical axis of the objective lens. The objective lens used is an HCX PL FLUOTAR L objective lens from Leica Microsystems, Germany with a magnification of 63$\times$ and a numerical aperture of 0.7. This objective lens provides a correction ring for spherical aberrations and a working distance of 1.8 to 2.6mm. The axial position of the focal plane can be adjusted roughly with a custom-built manual translating stage and the fine adjustment is done with a piezo scanner MIPOS 200 from Piezo Systems Jena GmbH, Germany. The assembled objective lens with the scanning device is mounted under the upside down mounted cryostat, like shown in figure 2.1.

2.2 Beam scanning system

The scanning in the lateral direction is provided by a beam scanning assembly because the huge weight of the cryostat inhibits a stage-scanning concept. For the appropriate beam scanning, a tilting mirror scanner is installed - PSH 10/2 SG from Piezo Systems Jena GmbH, Germany. To assure a constant intensity distribution across the back aperture of the objective lens and an appropriate tilting of the beam for lateral scanning of the specimen, the object plane of the scanning mirror has to be translated

to the pupil plane of the objective lens. Therefore a 4f imaging system is assembled in the manner shown in figure 2.2. Here the incoming beam is tilted (red line) with respect to the central beam (green line), which is translated into lateral displacement of the PSF in the focal plane (inset on the right hand side).

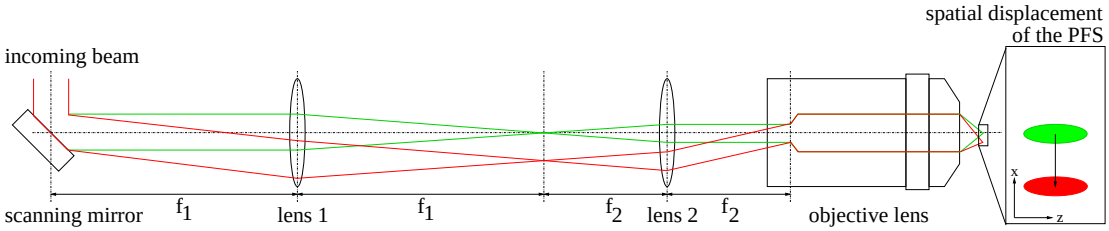

Figure 2.2: A beam scanning schematic which deploys 4f imaging. The displacement of the PSF in lateral direction is shown in the inset on the right hand side.

2.3 Optical setup

The other aspects of the technical assembly are orientated on previously built STED setups, which have been published in more detail in the following theses [37, 38]. The setup contains mainly four parts, which are schematically drawn in figure 2.3 and described in detail in the following.

Excitation light source

The excitation of the fluorescence is provided by a pulsed 532nm, 80MHz laser diode (PicoTA from Picoquant, Germany). The laser diode can be triggered by an external signal, which assures the temporal alignment of the excitation and the STED pulses. The excitation beam is spatially filtered by a 5m long single mode fiber (Thorlabs Inc., USA), which provides in combination with an achromatic lens a collimated beam with a plane phase distribution. The pulse width of the excitation is around 80ps, the value is measured with a fast photo multiplier tube (Hamamatsu, Japan, temporal resolution of 35ps) and a single photon counting card SPC730 (Becker & Hickel, Germany). The polarization of the excitation light is chosen to be linear and parallel with respect to the STED beam polarization for optimal STED efficiency. During the early stages of this project, a pulsed 470nm laser diode (PicoQuant, Germany, 80MHz, pulse width 100ps) is deployed instead of the 532nm laser source.

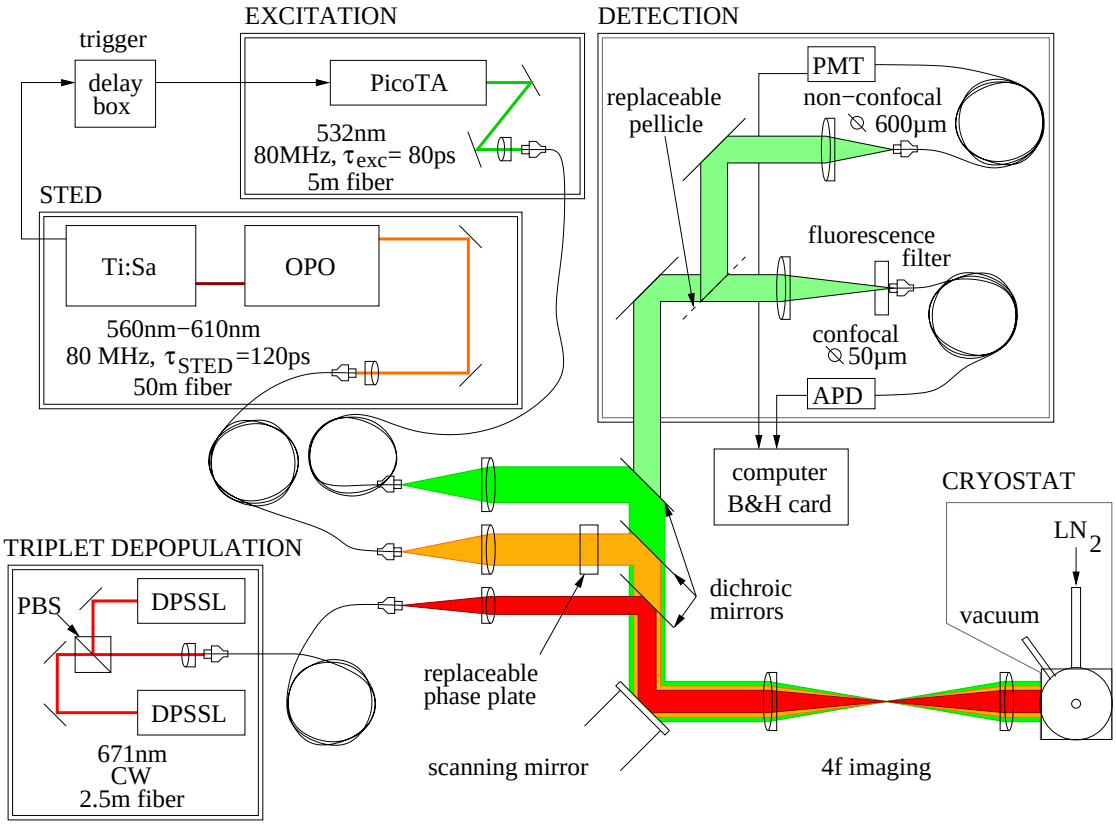

Figure 2.3: A schematic of the STED setup with an excitation laser, an STED laser and an additional laser for triplet depopulation and a cryostat. For detailed schematic of the cryostat, see fig. 2.1.

STED light source

The STED beam is provided by an optically pumped oscillator (OPO, APE, Germany). Here, a particular Ti:Sa wavelength (from MaiTai laser, Spectra Physics, Germany) at 80MHz is used with two non-linear processes to produce a new wavelength in the visible range of the light spectrum. The OPO wavelength is tunable in the range from 560nm to 610nm. The pulses have a width of several tens of femtoseconds. However, the necessary pulse widths for optimal STED microscopy lie above 100 picoseconds. Therefore the OPO pulses are stretched with a single mode fiber of 50m length (Schäfter und Kirchhoff, Germany), which produces a pulse widths of around 120 picoseconds. The single mode fiber also filters the laser mode spatially and provides a collimated beam in combination with an achromatic lens. A laser power controller (LPC, from BEOC, USA) is used to control the intensity of the STED laser (not shown in fig. 2.3 for simplicity). The polarization of the STED beam is chosen to be linear due to the constriction of the semi-circular π radians phase shift mask. The phase mask is mounted on a replaceable holder, so that the shape of the STED PSF can then be switched between a single diffraction limited spot for the spectroscopic measurements, and a semi-circular π radians retarded 1D doughnut for the resolution enhancement measurements, respectively.

The optimal STED efficiency depends on the temporal alignment of the excitation and the STED pulses. Therefore, a 80MHz seed signal from the Ti:Sa laser system is transferred to a time delay box (see fig. 2.3). The appropriately delayed signal (the delay time can be tuned with the resolution of 4ps) is used to trigger the excitation source. The fine adjustment is done by measuring the fluorescence depletion due to STED of a fluorescent sample as a function of the delay time. This is shown in figure 2.4, where the excitation pulse is fixed and the STED pulse is swept in time. The maximum STED efficiency is reached when the STED pulse immediately follows the excitation pulse. For a delay of more than 10ns, the STED efficiency vanishes completely due to short fluorescence lifetimes of 2-3ns [37].

Triplet depopulation light source

A third laser source is used to tackle the triplet population issue at low temperatures. The deployed lasers are diode pumped solid-state lasers (DPSSL) with wavelength 671nm and 300 mW of total power in CW mode (Shanghai DremLasers, China and Alphalas, Germany). To raise the total power, two lasers are coupled into one 2.5m long single mode fiber (Schäfter und Kirchhoff, Germany) with polarization alignment perpendicular with respect to each other. This provides a nearly circularly polarized light after the fiber. The use of the single mode fiber and an achromatic lens provides a collimated beam and thereby produces a single, diffraction limited spot. The triplet

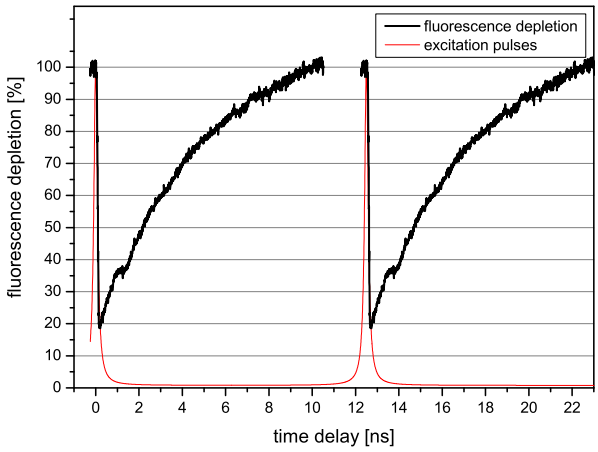

Figure 2.4: The fluorescence depletion due to STED as function of the time delay between the excitation and STED pulses (black line). The repetition of the excitation pulse position is shown as red line. The optimal delay time is around several ps.

depopulation intensity is controlled by a LPC.

Detection

The signal detection can take place in two different modes: (1) confocal and (2) non-confocal configuration.

The confocal configuration is used for an efficient detection of the fluorescent light originating from the focal plane. Therefore, the collimated fluorescence beam is focused with an achromatic lens onto a multimode fiber with the appropriate diameter of 50μm. The interplay of the fiber diameter (pinhole size) and the focal length of the detection lens dictates the confocal condition [27]. The fluorescence contribution is separated from the laser reflections with an appropriate fluorescence filter. The harvested fluorescence light is detected with an avalanche photo diode (APD, IdQuantique, Switzerland), which translates the single photon impacts into electronic TTL pulses.

The non-confocal configuration is used for the spatial alignment of the diffraction limited focal spots. Therefore, highly reflective gold spheres with 150nm in diameter (150nm gold colloids from BBInternational, UK) are scanned with the laser PSFs. The scattered light is then deflected by a replaceable pellicle beam splitter (Thorlabs Inc., USA) and focused onto a multimode fiber with 600μm diameter. This aperture reduces the background noise that does not originate from the focal plane of the objective lens.

The size of the aperture is chosen to be twelve fold size of the confocal condition and fulfills the non-confocal requirements. The detected light is then translated into electronic TTL pulses by a photo multiplier tube (PMT, Perkin Elmer, USA).

The electronic TTL pulse sequence is recorded by a single photon counting PC card SPC730 (from Becker & Hickel, Germany). This card provides the ability to measure the arrival time histograms of detected photons (time correlated single photon counting, TCSPC). Therefore the delay time between the TTL pulse on the detection side and the laser pulse is recorded for every detected photon. Adding these delay times in one graph provides the arrival time histogram of the detected photons. This measurement technique can be used to obtain the fluorescence lifetime and to distinguish between the fluorescent and the non-fluorescent photons (e.g. scattering) due to different temporal characteristics. This ability is used in this work for the removing the contribution of the laser scattering, which originates from the refractive index mismatch in the samples (for detailed description see the appendix A).

2.4 PSF engineering

For optimal STED efficiency, the diffraction limited spots from all lasers has to be spatially aligned. To assure the spatial alignment in all three dimensions, every sample contains sparsely distributed gold spheres for the non-confocal alignment of the PSFs. First, the aberrations are eliminated by consequent observation and optimization of each PSF. The spatial alignment of the PSFs is tuned in the lateral direction with the dichroic mirrors and in the axial direction with the z-position of the particular achromatic lenses.

For the spectroscopic measurements, like the determination of the STED efficiency, the anti-Stokes excitation or the influence of the triplet population to STED microscopy, all the PSFs are adjusted in same manner, like in figure 2.5. This configuration provides the optimal spatial alignment of the diffraction limited spots.

As already described on page 6, a modified STED intensity with a zero is necessary for the resolution enhancement in STED microscopy. The STED intensity spot is modified by a semi-circular π-retardation phase mask, shown in figure 2.6(c). Here, half of the STED beam travels through an additional layer with higher refractive index than the remaining beam part. This phase mask produces an intensity distribution of two neighboring spots with a valley in between (central PSF in figure 2.6(a)). At optimal conditions, the minimum value of this valley is zero. For destructive interference in the focal plane, the phase of the retarded part of the STED beam needs to be exactly π radians. This is controlled by the thickness of the layer as well as by the refractive

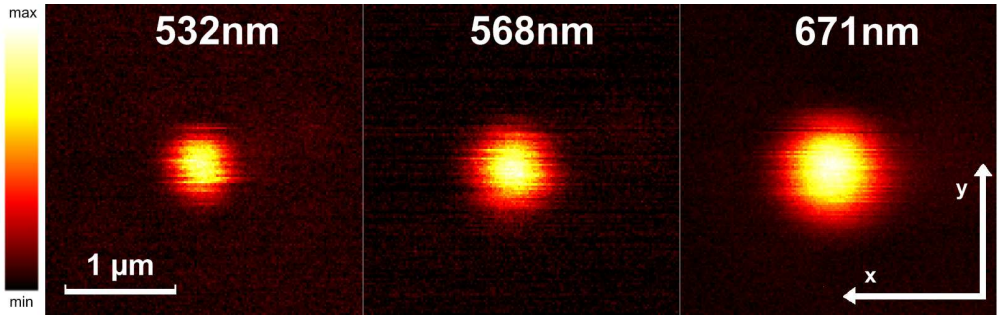

(a) Diffraction limited spots alignment of excitation (532nm), STED (568nm) and triplet depopulation (671nm) laser sources.

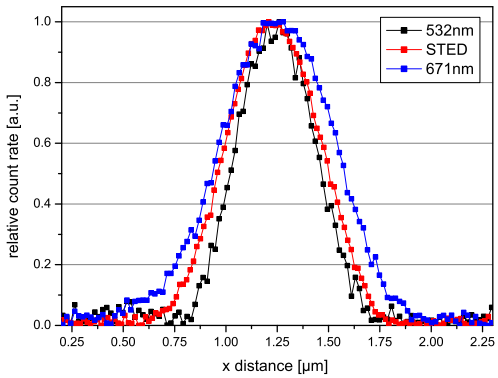

(b) Line scan through overlapped images in figure 2.5(a).

Figure 2.5: The PSF alignment in lateral dimension for spectroscopic studies.

index of the utilized material. The layer thickness is given by

$$d = \frac{\lambda_{\mathrm{STED}}}{2\Delta n} \tag{2.1}$$

where Δn is the difference between the refractive index of the material and air. The phase plates were prepared by thermal evaporation and deposition in vaccum of the MgF_2 with refractive index $n_{\mathrm{layer}} = 1.367$ for the wavelength of 563nm [39].

2.5 Experimental prerequisites

Sample preparation

The daily assembly of the cryostat with the optical setup causes slightly different tilting angles of the sample with respect to the optical axis of the objective lens. This

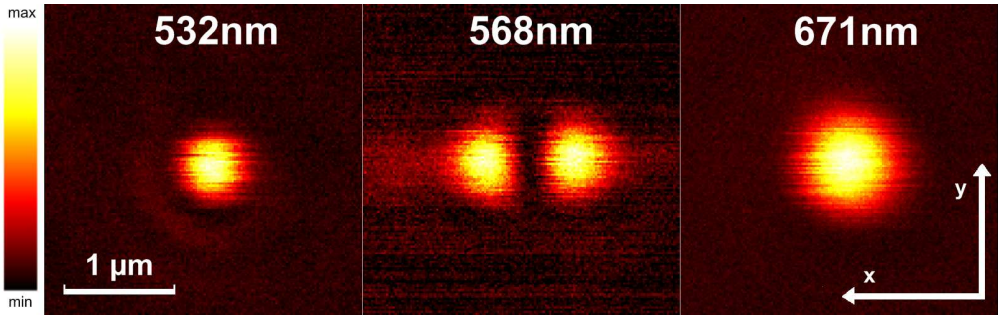

(a) STED intensity distribution with a semi-circular π phase mask (568nm) aligned with excitation (532nm) and triplet depopulation (671nm) spots.

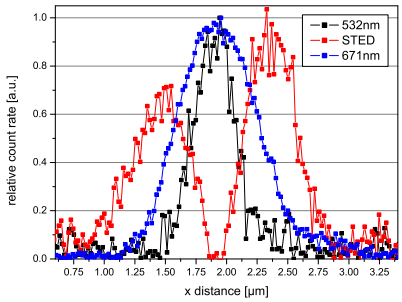

(b) Line scan through overlapped images in figure 2.6(a)

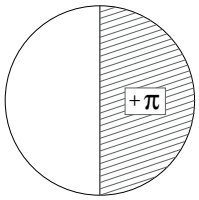

(c) The semi-circular π radiant phase retardation mask.

Figure 2.6: The PSF alignment in lateral dimension for resolution enhancement.

fact necessitates an in-situ[1] PSF probing. Therefore, a sample always contains besides the fluorescent specimen of interest, a sparsely distributed gold colloids for the PSF adjustment.

The clean cover glass is incubated with a poly-l-lysine solution (Sigma-Aldrich Chemie GmbH, Germany) for 10 min and then the residual solution is sucked off. The poly-l-lysine treated surface is incubated with a diluted aqueous gold colloid solution (10 parts water plus 1 part gold colloid stock solution) for further 10 min, the residual solution is sucked off again. This assures a gold colloids distribution with the spatial distance of 10-20 μm in between. As a final step, the fluorescent specimen is attached to the surface, mounted with a drop of glycerin and covered with a second clean cover glass.

Consequently the sample is attached to the sample holder with glycerin to assure good thermal contact. Because the cover lid is only held by the vacuum inside the vacuum chamber, the cryostat is evacuated very gently to avoid the mounting medium from being sucked off. The cryostat with slightly reduced pressure inside the vacuum

[1] in the place *lat.*

chamber is now mounted onto the stage.

PSF and detection adjustment

First, any casual present aberrations have to be eliminated. Usually two kinds of aberration were observed during the CryoSTED project - (1) spherical aberrations and (2) coma aberrations. The usually observed aberrations are shown in figure 2.7. Luckily,

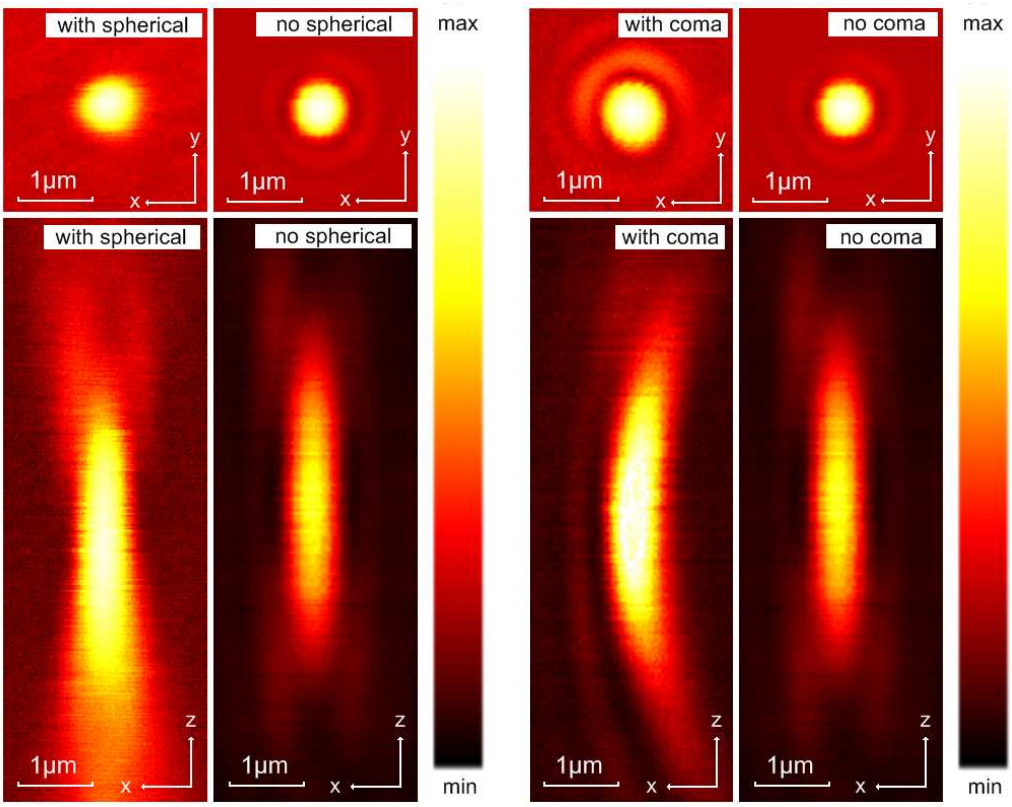

(a) The correction for the spherical aberration is provided by the correction ring of the objective lens HCX PL FLUOTAR L (Leica Microsystems, Germany).

(b) The correction for the coma aberration is made by tilting the mounting stage with respect to the optical axis of the objective lens with a custom-made tilting device.

Figure 2.7: Elimination of the commonly observed aberrations in the CryoSTED project. The PSFs are recorded with non-confocal PMT detection.

both aberration can be corrected. The correction of the spherical aberration is done by adjustment of the correction ring of the objective lens. For the elimination of the coma aberration, the angle of the sample inside the cryostat with respect to the optical axis of the objective lens has to be adjusted to 90°. This ability is provided by a custom made tilting mount with two degrees of freedom. Both adjustments are iteratively performed and the quality of the PSFs is observed by eye in wide-field illumination.

After the elimination of the aberrations, the three PSFs (excitation, STED and triplet depopulation spots) are adjusted for the appropriate overlap at room temperature. To this end, the reflection of the 150nm big gold colloids in the non-confocal detection mode with a PMT is observed for each laser source. After the alignment steps fulfill the requirements, the confocal detection is adjusted roughly by maximizing the fluorescence signal of the APD.

Cooling of the sample

The sample is cooled by a constant cold nitrogen gas flow, which is provided by a membrane pump. The temperature on display is observed and if the temperature is below the freezing point of the mounting media, the turbo molecular pump is switched on. The cause for this is that under high vacuum conditions, the liquid mounting medium evaporates completely, and thereby causes the loss of thermal contact. Thus the display temperature needs to be less then 270K for aqueous solutions, less then 260K for glycerin and less then 160K for ethanol. In case of poly-vinyl-alcohol (PVA) the mounting medium is rigid at room temperature. Therefore, in principle, the turbo molecular pump can be switched on before cooling. After the vacuum reaches common values below 1×10^{-5} mbar, the sample is cooled to lower temperatures.

After the cooling process, the alignment of the PSFs is checked again and optimized if necessary. The confocal fluorescence detection is optimized to maximum signal.

Chapter 3

Experimental results

The utilization of liquid nitrogen or even lower temperatures in fluorescence microscopy brings along new challenges. Besides the technical efforts, like the need for vacuum technology and the high mechanical stability requirements, one has to solve the photophysical problem of high triplet population at low temperature conditions [40]. The triplet population build-up leads to a reduced brightness of fluorescence and increases the bleaching probability [36, 41]. The interference of the triplet population within the STED microscopy has been hardly studied to date. The major tasks for this work are the characterization of the influence of the triplet population within STED microscopy and to seek a practical solution for minimizing the triplet population.

3.1 Triplet population

Basic considerations on the triplet state

The electron configuration of fluorescent dyes and its interaction with photons is mainly given by the delocalized π-electrons [10]. These form a regular electron cloud and propagate along the consolidated π-orbital system. The wave functions describe the characteristic behavior of the electron system and their eigenvalues provide an energy spectrum of the fluorescent molecule. A common way to visualize the energy spectrum is the Jablonski diagram. A qualitative Jablonski diagram highlights the energetic configurations and the pathways of possible transitions between them as shown in figure 3.1. The energy diagram of a fluorescent molecule usually consists of two kinds of the electronic configurations: a singlet configuration with a zero spin sum $\sum_i \vec{s}_i = 0$, and a triplet configuration with $\sum_i \vec{s}_i \neq 0$. A transition between them requires a spin flip, which is forbidden from the basic quantum mechanical model.

However the crossing probability can be increased by the introducing of small distortions, e.g. by the addition of heavy atoms to the molecular structure [42].

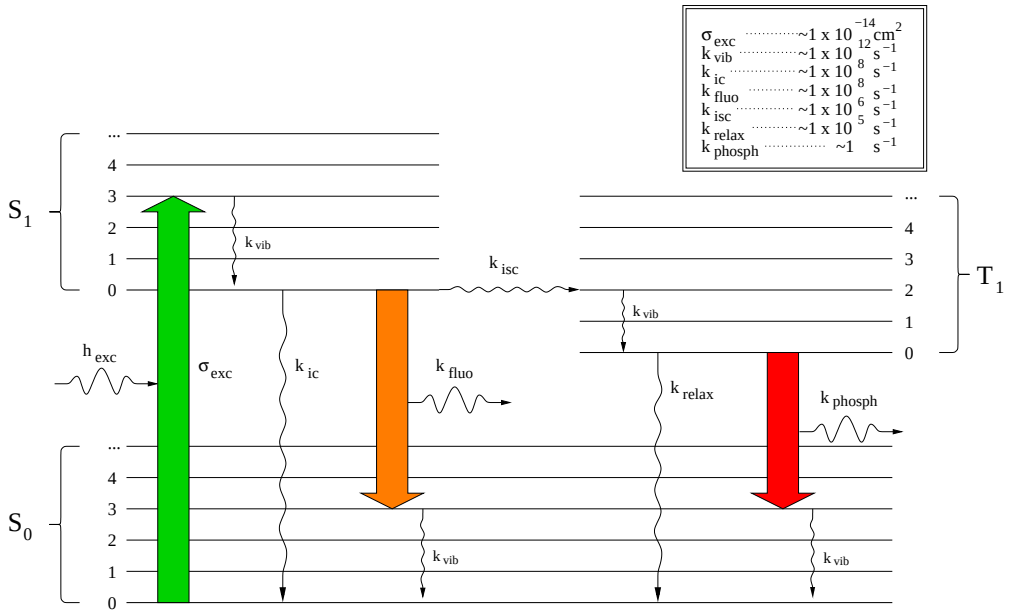

Figure 3.1: Jablonski diagram with the electronic singlet and triplet systems and the significant transitions. Every electronic state splits into vibrational states. The inset shows the typical ranges for presented rate constants, for abbreviations see corresponding text.

In the ground state S_0, the molecules have the singlet configuration and can be excited to higher singlet states S_1, S_2, ..., S_N by absorbing a photon with the corresponding wavelength. The amount of excited molecules is given by the product of the excitation cross section and the photon flux $\sigma_{exc}h_{exc}$. The relaxation of the high energetic, excited states $S_{(N\geq 2)}$ to the first excited state S_1 is given by the Kasha rule [43]. These relaxations are very fast, the rates are in the same range as the vibrational relaxations k_{vib}, they relax within several hundreds femtoseconds into the S_1 state. In the fluorescent molecules, the first excited state S_1 has several channels for relaxation, as highlighted in fig. 3.1. On one hand, the molecules can cross the $S_1 \rightarrow S_0$ transition by sending out a photon with the fluorescence rate k_{fluo}, on the other hand they can relax radiationless into the S_0 state via internal conversion rate k_{ic}. The third pathway for the molecules leads to the triplet state T_1 with a intersystem crossing rate k_{isc}. The relaxation from the T_1 state into the ground state S_0 takes place in two manners: (1) the molecule sends out a photon with a phosphorescence rate k_{phosph} or (2) it relaxes radiationless with the rate k_{relax}. Because the transition $T_1 \rightarrow S_0$ requires a spin flip, both rates are slower than the singlet-singlet transitions (compare inset of fig. 3.1).

The temporal evolution of the state populations in the Jablonski diagram is de-

scribed by the rate equations with the significant rates from fig. 3.1:

$$\frac{d}{dt}\mathrm{S}_1(t) = -(k_{fluo}+k_{ic}+k_{isc})\,\mathrm{S}_1(t)+\sigma_{exc}h_{exc}\mathrm{S}_0(t) \tag{3.1}$$

$$\frac{d}{dt}\mathrm{T}_1(t) = k_{isc}\mathrm{S}_1(t)-(k_{relax}+k_{phosph})\,\mathrm{T}_1(t) \tag{3.2}$$

$$\frac{d}{dt}\mathrm{S}_0(t) = (k_{fluo}+k_{ic})\,\mathrm{S}_1(t)-\sigma_{exc}h_{exc}\mathrm{S}_0(t)+(k_{relax}+k_{phosph})\,\mathrm{T}_1(t) \tag{3.3}$$

To obtain the population numbers in equilibrium, the rate equations are solved for the steady state condition (temporal derivatives equal zero). The solution for the triplet population T_1 in case $k_{fluo}+k_{ic} \gg k_{isc}$ (compare inset of fig. 3.1) is given by expression:

$$\mathrm{T}_1 = \frac{k_{isc}}{k_{relax}+k_{phosph}+k_{isc}} \tag{3.4}$$

The graphical presentation of expression 3.4 in figure 3.2 shows the characteristic behavior of the triplet population with the change of k_{relax}. It can be seen that the reduction of relaxation constant k_{relax} by 2-3 orders of magnitude comes along with the triplet population build-up, where 90% of molecules are trapped in the triplet state.

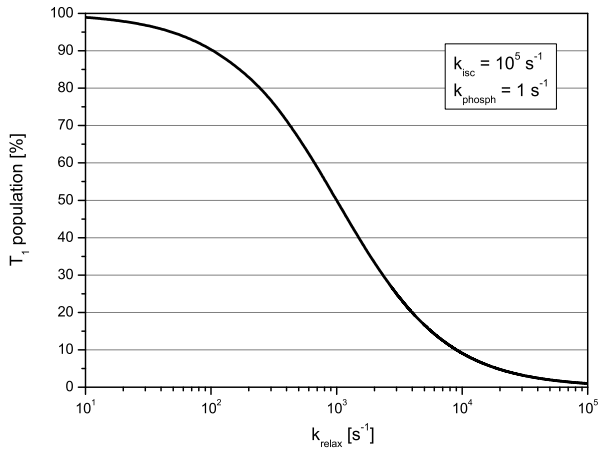

Figure 3.2: Relative triplet population as function of k_{relax} calculated from expression 3.4

Triplet population build-up at 76K

The properties of different dyes are studied at 76K with particular attention to the triplet state population. The obtained results show the similar characteristics for all

the dyes investigated, which underlines the general validity of the concepts presented in the following.

The fluorescence behavior of the fluorescent marker Rh123 diluted in glycerin at 76K is shown in figure 3.3. The time trace in the upper graph shows the fluorescence response to a certain temporal excitation pattern. The sample is illuminated with a 470nm, 80MHz laser spot for 50ms, followed by 50ms long dark period, with the subsequent repetition. The excitation pattern is shown via the green-shaded areas in the background of figure 3.3.

When the excitation shutter opens for the first time, the fluorescence appears at its initial value. From there on, a monotonous decrease in fluorescence can be observed. After nearly 40ms, the value of the detected fluorescence reaches a saturation level around 20% of the initial fluorescence value. After the dark period, the detected fluorescence rises to 30% of the original value and, again, decreases to the plateau level of around 20%.

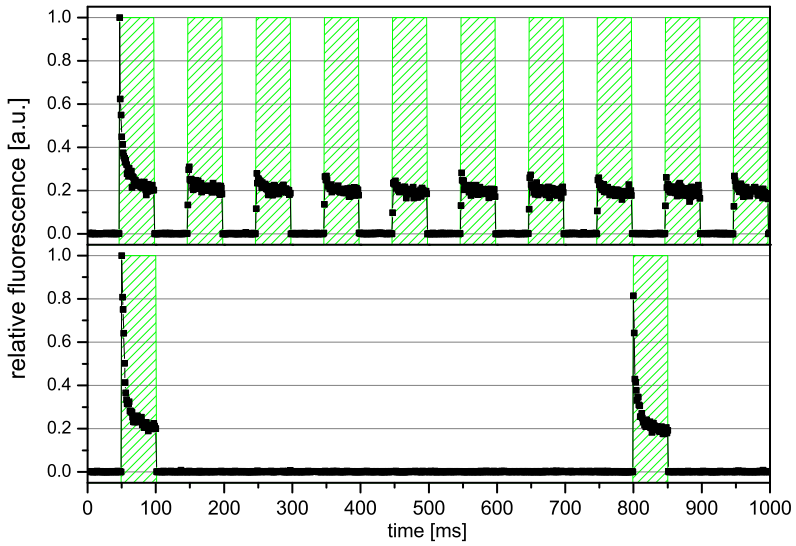

Figure 3.3: Triplet population of Rh123 at 76K and its behavior on the excitation pattern (green-shaded areas) with different dark periods. (sample: Rh123 diluted in glycerin, excited with 470nm 80MHz laser diode.)

The decrease of the detected fluorescence is interpreted as build-up of a dark molecule population within the excitation spot. Thereby the plateau level of fluorescence is given for the equilibrium condition between the build-up and the relaxation of the triplet population. The amount of molecules, trapped in the dark (triplet) state, is estimated by the difference of the initial fluorescence and the residual plateau level.

Thus at 76K nearly 80% of the molecules inside the excitation spot are trapped in the triplet state after reaching the steady state condition. The partial recovery of the fluorescence around 10% after a 50ms dark period indicates that the relaxation time of the triplet population is dramatically increased compared to room temperature conditions.

The lower trace in figure 3.3 shows the fluorescence behavior for the same sample with a changed excitation pattern. Here the dark period between the excitation is increased to 700ms. During the first excitation period, the fluorescence shows the same behavior as described before: the detected signal decreases from its initial value to the plateau level within 40ms. After a dark period of 700ms, the fluorescence signal has recovered to ~80% of the original value from the first excitation period. During the second excitation period, the fluorescence again decreases to the plateau level of 20%.

In figure 3.3, the presented traces with different temporal excitation patterns indicate a dark state population at 76K with a lifetime between 50ms and 700ms. This dark state is supposed to be the triplet state T_1. The lifetime of the triplet population at 76K is measured by varying the dark period between two excitation periods. The amount of molecules trapped in T_1 is estimated from the difference of the initial and the remaining fluorescence level. The measurements for different dark periods are carried out at the same position of the sample, the contribution of the possible photo-bleaching is corrected from the remaining fluorescence level.

The data for different times between the excitation periods are presented in figure 3.4. The triplet population curve (black squares) decreases exponentially with increasing waiting times between two excitation periods. The exponential decay fit for the triplet population delivers a lifetime of 511ms. The contribution of the bleaching (red dots) shows a decrease of 11% from the original fluorescence value.

The data presented in figures 3.3 and 3.4 show a fluorescence decrease during the excitation periods to a saturation level plateau within 40ms. The cause for the fluorescence reduction is a build-up of the dark state, which is highly favored by the slow relaxation time of this dark state. This dark state is supposed to be the triplet state T_1, but the measurements of the fluorescence decrease cannot rule out the existence of an other dark state, which has been reported for a specific rigid matrix [44].

The results can be nicely reproduced for every fluorescent marker that we have tried out during this project. The dyes with known high intersystem rate (EosinB and Atto465) have shown high triplet population build-ups at 76K, as well as the dyes with known low triplet yield at room temperature (e.g. Rh110, Rh123 and Rh6G). The fluorescent proteins (GFP and EYFP) have also shown similar behavior at 76K. Independent from the fluorescent marker choice, the CryoSTED microscopy faces very high triplet population values of around 80% and 90%. Thus a study of the inter-

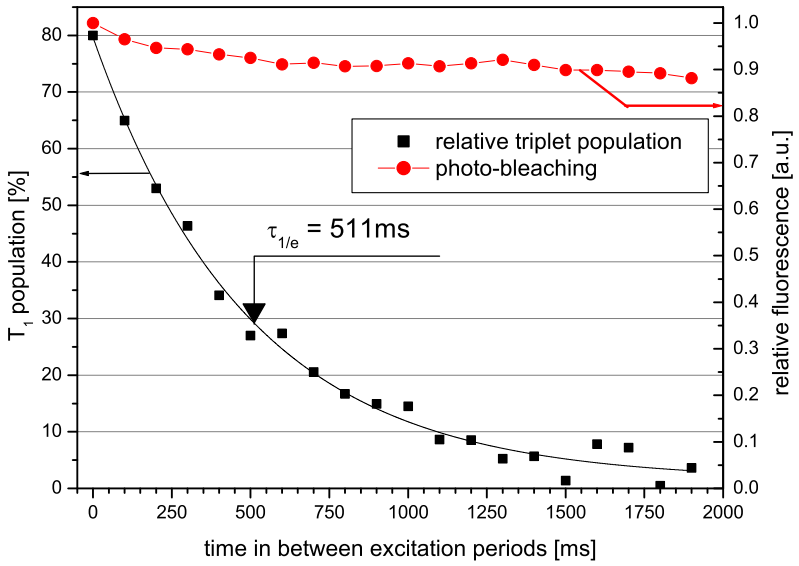

Figure 3.4: Left ordinate: Spontaneous triplet relaxation of Rh123 dye at 76K as function of relaxation time. Right ordinate: Bleaching approximation from fluorescence signal remaining after triplet population. (sample: Rh123 diluted in glycerin, excited with 470nm 80MHz laser diode. Triplet population is estimated from peak height value.)

ference between the triplet state population and the stimulated emission depletion is neccessary.

Influence of the triplet population in CryoSTED microscopy

The study of interference of the triplet population with the STED photons at 76K utilizes a combination of a common STED microscope setup with pulsed laser sources and a cryostat as described in section 2. The investigated fluorescent markers are diluted in glycerin and polyvinylalcohol (PVA), and the fluorescent proteins in PBS-buffered water. The diffraction limited excitation and de-excitation laser spots are spatially aligned for optimal STED efficiency. The use of pulsed laser sources necessitates a temporal alignment of the pulses. This alignment was performed by the tuning of the electronic time delay between the excitation and de-excitation pulses.

The interaction between the triplet population and the STED photons can be visualized most prominently, when the contribution of the stimulated emission depletion of the first excited state S_1 is ruled out. The fluorescence lifetime of the dyes used is around 2-3 nanoseconds, and the lifetime of the triplet state is 0.5 seconds. Thus

a stimulated emission depletion pulse tuned to arrive 10ns after the excitation pulse can only interact with the triplet population (compare fig. 2.4). Commonly, the temporal alignment in STED microscopy is optimized for the best STED efficiency when the STED pulse immediately follows the excitation pulse [24, 45]. Both configurations are tested on the fluorescent dyes on purpose to highlight the most prominent differences.

Figure 3.5 shows a typical behavior of the fluorescence on STED illumination at 76K. This particular graph shows the fluorescence development of green fluorescent protein (GFP) for 10ns delayed (black squares) in contrast to several picoseconds delayed (red squares) STED pulse. The fluorescence signal in both time traces increases as the excitation is switched on. The illumination with the STED light causes the fluorescence signal to increase by a factor 1.4 compared to the initial fluorescence value in the case of 10ns delayed STED pulse (black squares). When the STED light is switched off, the fluorescence signal is reduced. The following repeat of the STED illumination show the same picture: when the STED light is applied to the sample, the fluorescence signal is increased. Since the time trace was taken on the same sample position, an overlaying signal reduction due to photo-bleaching is observed.

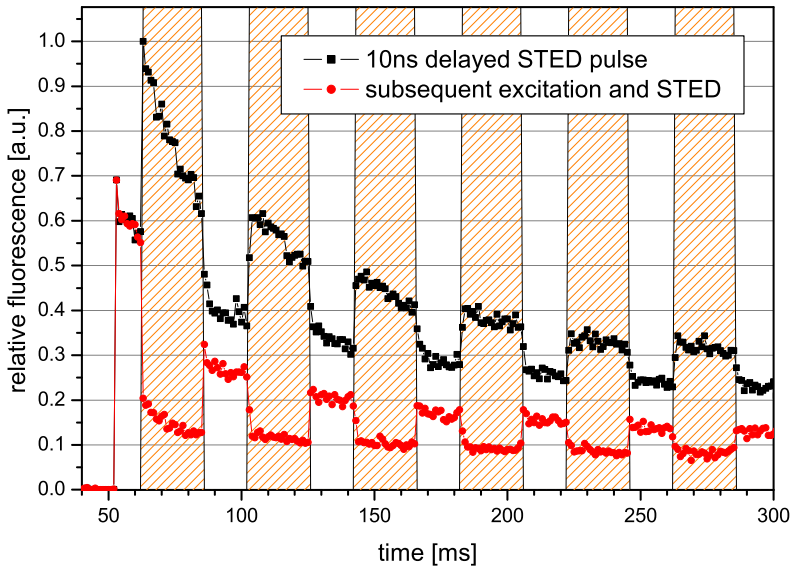

Figure 3.5: STED applied at 76K for different time delays between excitation and STED pulses. (sample: GFP in PBS-buffered water, excited with 470nm 80MHz laser diode and de-excited with 565nm 80MHz OPO system.)

The fluorescence trace with optimal temporal excitation and STED pulse alignment shows a reduction of the fluorescence signal (red dots in fig. 3.5), the fluorescence

signal is instantly reduced to 40%. When the STED illumination is interrupted, the fluorescence signal increases. The general reduction of the fluorescence due to photobleaching is also observed. The fluorescence deviation caused by the STED effect vanishes with the number of following STED illumination periods.

The fluorescence trace in figure 3.5 with the 10ns delayed pulses arrangement show an increase in fluorescence. The direct excitation by the STED pulse was excluded in a separate measurement, where the sample was illuminated with the STED beam only. Therefore the fluorescence increase can be immaculately accounted to the interference of the STED photons with the triplet population. Somehow, the molecules which are trapped in the T_1 state absorb a STED photon, and thus return to the fluorescent S_1 state. The interpretation of the trace with the optimal excitation and STED pulse alignment is more difficult, because the fluorescence reducing STED effect overlays the interaction of particular STED photons with the triplet population. The achieved fluorescence depletion of 60% also indicates a negative influence of the triplet population within STED microscopy in a sense of reduced STED efficiency.

The presented fluorescence behavior in STED microscopy at 76K has proved to be general for all dyes used. As long the triplet population is present, an increase of the fluorescence signal has been observed. The fluorescence signal gain is caused by the triplet depopulation, stimulated by absorption of STED photons. Thus a negative influence on the STED effect, in particular worse signal to noise ratio and a reduced STED efficiency, can be expected. Thus the presence of the triplet population is expected to reduce the resolution enhancement in STED microscopy, referring to the dependency of the resolution enhancement on STED efficiency. The optimization of the STED microscopy in terms of the resolution enhancement necessitates an elimination of the negative influence of the triplet state. A determination of the pathway for the triplet depopulation is necessary in order to find a practical solution for the triplet population issue.

Optical stimulated pathways from triplet to singlet

The triplet population issue at low temperatures can be solved by illumination of the trapped molecules with light, as the measurements in figure 3.5 already have suggested. A closer look at the Jablonski diagram suggests only two possible optically driven pathways from the triplet into the singlet states: a direct stimulation of the $T_1 \rightarrow S_0$ transition and a $T_1 \rightarrow T_N$ transition with subsequent intersystem crossing to the high energy singlet states S_N.

An experimental test for the suggested pathway from the state T_1 to S_1 via higher excited states T_N, S_N is the observation of the fluorescence from the S_1 state during the triplet depopulation. A triplet population of the fluorescent marker Rh6G is prepared during excitation periods with the 532nm, 80MHz laser spot (green-shaded areas),

followed by dark periods without the excitation illumination. The triplet population prepared in that manner is then illuminated with a 671nm, CW laser spot (red-shaded areas) at maximum intensity of 5.3MW/cm^2. To rule out the possibility of the two photon excitation, the sample is illuminated with 671nm after a dark period of 520ms again (red-shaded area at around 950ms in fig. 3.6).

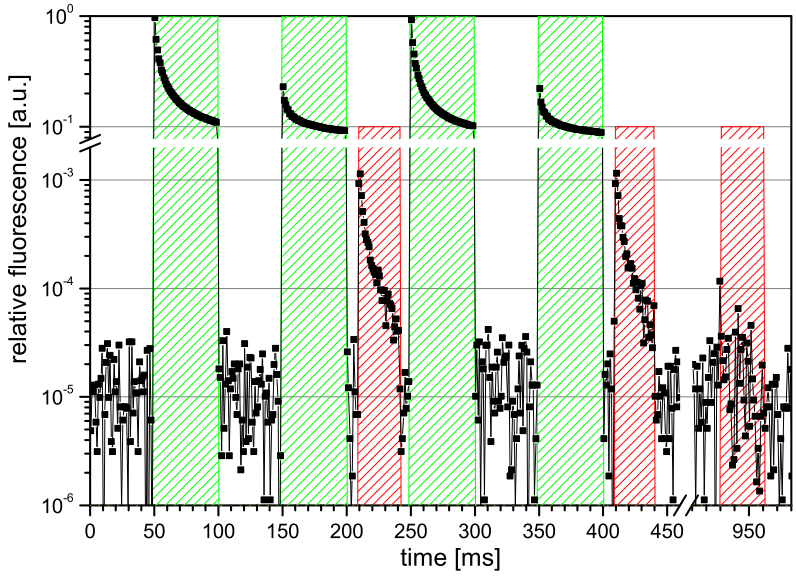

Figure 3.6: Rhodamine6G shows a decrease of one order of magnitude in fluorescence due to triplet population build-up. The illumination with 671nm causes fluorescence from first excited singlet state. (sample: Rh6G in glycerin, excited with 532nm 80MHz laser diode, triplet depopulation with 671nm CW laser at 5.3MW/cm^2.)

The fluorescence trace in figure 3.6 shows the behavior of Rh6G at 76K. During the excitation period (first green-shaded area), the fluorescence decreases to a residual fluorescence plateau of 11% of the initial signal value. During the second excitation period, the fluorescence time trace starts at 23% of the original value, and decreases to the plateau again. An illumination of the sample with the 671nm laser spot causes a fluorescence signal (within the red-shaded areas in fig. 3.6), which is suppressed in its height by three orders of magnitude compared to the original fluorescence value. The additional illumination of the sample at the end of the measurement shows no significant fluorescence signal.

In the presented fluorescence trace the decrease of the detected fluorescence is ascribed to the triplet population build-up (compare the measurement in fig. 3.4). For

the combination of 532nm excitation source and Rh6G, 89% of molecules are trapped in the dark triplet state. The second excitation period shows that the amount of the triplet is reduced to 77% after 50ms relaxation time, which is in very good agreement with the triplet population decay with a lifetime of 500ms. The most interesting fact is the appearance of fluorescence during the illumination with 671nm laser spot. A possible contribution due to two photon excitation is excluded by the illumination of the sample with the 671nm spot without present triplet population. Thus the observed fluorescence caused by 671nm light can only originate from the triplet population.

The shown measurements unveil the pathway of the optical stimulated triplet-singlet transition over the higher excited states $\mathrm{T_N}$, $\mathrm{S_N}$. This measurements also provide a practical solution to the triplet population issue in CryoSTED microscopy. We suggest the utilization of an additional red-shifted laser source on purpose to effectively depopulate the triplet state. This technique adds some benefits to STED microscopy at 76K, especially the enhanced brightness of the fluorescence markers due to the strongly reduced retention in the dark triplet state.

The following sections (see pages 33 and 50) will present the benefits for confocal imaging at 76K in terms of brightness enhancement and the influence on the STED efficiency.

Triplet depopulation for imaging at low temperatures

The fluorescent specimen contains sparse diluted silica spheres of 65nm diameter filled with Atto532. Glycerin is chosen as mounting medium due to its small refractive index mismatch compared with glass ($n_{\mathrm{glycerin}} = 1.47$, $n_{\mathrm{glass}} = 1.56$) and its glassy-like freezing properties [46]. The excitation (532nm, 80MHz) and triplet depopulation (671nm, CW) laser spots are spatially aligned for optimal triplet depopulation. The confocal images are taken sequentially line by line with alternating 671nm illumination. First, a line in the fast scanning axis is scanned under the illumination with only the excitation spot; after that, the same line is scanned with the illumination of both, the excitation and the triplet depopulation spots. In that manner both pictures are taken parallel and this scanning mode eliminates the influence of slow drifts. The figure 3.7 shows a composition of typical images obtained at 76K.

The parallel obtained images of the Atto532 fluorescent beads in figure 3.7(a) show a dramatic brightness increase due to the triplet state depopulation of the Atto532 molecules. The intensity profiles along the white line are shown below in 3.7(b), the brightness enhancement for the two shown beads is about 7-8. The development of brightness increase as a function of the 671nm laser intensity is shown in the fig. 3.7(c). It shows the averaged values of brightness increase, obtained from many Atto532 beads. The curve shows an initial increase in the brightness due to the more efficient triplet depopulation, followed by small decrease in the brightness for larger

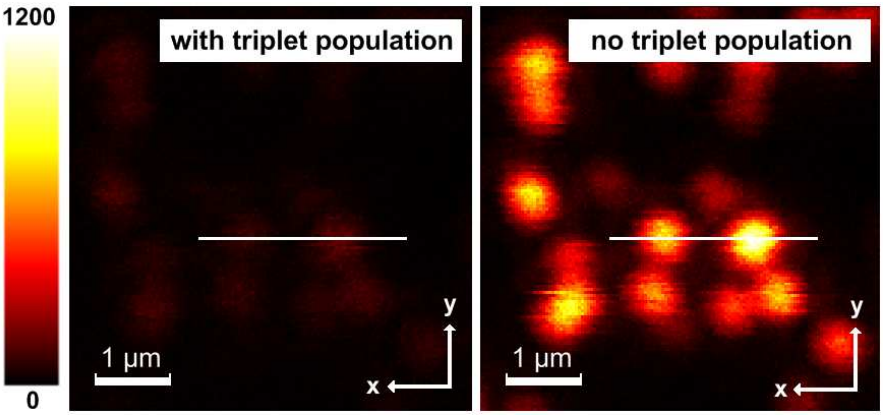

(a) Picture taken on silica beads with Atto532 at 76K. On left, the sample is illuminated with excitation laser source (532nm) only, on the right additionally a 671nm laser spot at 14.8MW/cm^2 is switched on.

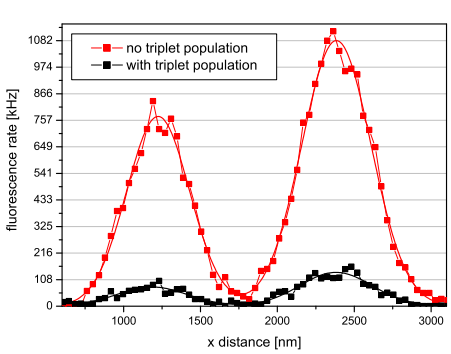

(b) A line profile in 3.7(a) across the white lines. The brightness enhancement provides sevenfold higher intensity counts.

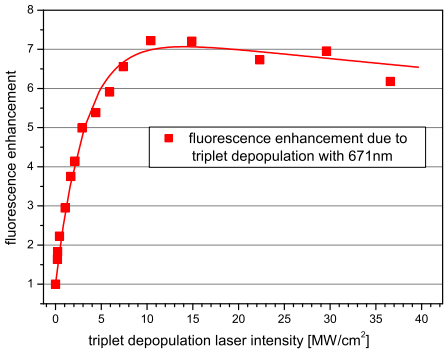

(c) Brightness enhancement due to triplet depopulation by 671nm light versus optical power determined over many beads.

Figure 3.7: Optically triggered triplet depopulation improves fluorescence imaging microscopy at liquid nitrogen temperatures. (sample: Atto532 spheres, 65nm in diameter, excited with 532nm 80MHz laser diode. Triplet depopulation with fiber-coupled 671nm CW.)

intensities due to photo-induced bleaching.

The presented results confirm the expected brightness enhancement in the fluorescence imaging at 76K. The triplet depopulation with 671nm laser source is sufficient and the saturation-like behavior indicates a completely empty triplet state under the presented conditions.

Conclusions on the triplet state at 76K

The triplet population build-up at low temperatures is an issue for fluorescence imaging microscopy in general. The presented results have been reproduced for several other fluorescent markers; all have shown, besides small deviations in absolute values, a triplet population at 76K. The amount of the molecules trapped in triplet state lies between 80% and 90% for all of the studied fluorescent markers. Therby the triplet population has huge negative influence on STED microscopy in terms of reduced signal-to-noise ratio and reduced STED efficiency.

The solution for the triplet issue at low temperatures is provided by the introduction of an additional laser spot, which is assigned particular to the triplet depopulation. The shown results confirm a complete triplet depopulation under the utilized conditions. A patent has been applied for for the here presented solution to the triplet population problem [47].

3.2 Anti-Stokes excitation

Thermal distribution of vibrational modes

The disadvantage associated with direct anti-Stokes excitation has prevented the utilization of STED wavelengths with optimal stimulated emission cross section to date. The applied STED intensities directly stimulate the $S_0 \rightarrow S_1$ transition and thereby compete with the fluorescence depletion process. At a certain wavelength and intensity, the anti-Stokes excitation just compensates the stimulated emission depletion and thus annihilate the resolution enhancement. A control of the anti-Stokes excitation by a conditional change can allow the appliance of the desired STED wavelengths and thereby increase the STED efficiency.

The energetically higher excited vibrational states of the S_0 state are accountable for the direct anti-Stokes excitation by the STED photons. Usually, the transitions from the excited vibrational states of the electronic ground state to a higher electronic state is strongly suppressed. However large intensities from several MW/cm^2 to few GW/cm^2 are applied to the samples in STED microscopy. Thus the very small excitation cross sections are compensated by the large photon flux h_{STED}.

Since the population of high excited vibrational states is thermal activated [42], a reduction of the temperature is a promising approach to reduce the anti-Stokes excitation. A Jablonski diagram in fig. 3.8, considering the two singlet states S_0 and S_1, shows the estimated occupation of the vibrational states at room temperature (red dots on the left hand side) and at liquid nitrogen temperature (blue dots on the right hand side). The reduced number of high excited, "'hot"' vibrational states at 77K therefore allows the utilization of STED wavelengths with larger stimulated emission cross section, than it is possible to date.

The occupation density of the vibrational states is given by the Boltzmann distribution [48]. The density f is a function of the energy E_{vib} of a particular vibrational state and of the thermal energy $k_B T$, where T is the temperature and k_B the Boltzmann constant:

$$f\left(E,T\right) = \exp\left(-\frac{E_{vib}}{k_B T}\right) \tag{3.5}$$

For the calculation of the anti-Stokes excitation cross section, we need to consider all occupied vibrational states, which have the probability to be lifted to the first excited electronic state S_1 by a STED photon. These are all vibrational states with energy $E_{cut} \geq E_{S_1-S_0} - E_{\lambda_{\mathrm{STED}}}$. The total number of the occupied states above the energy level

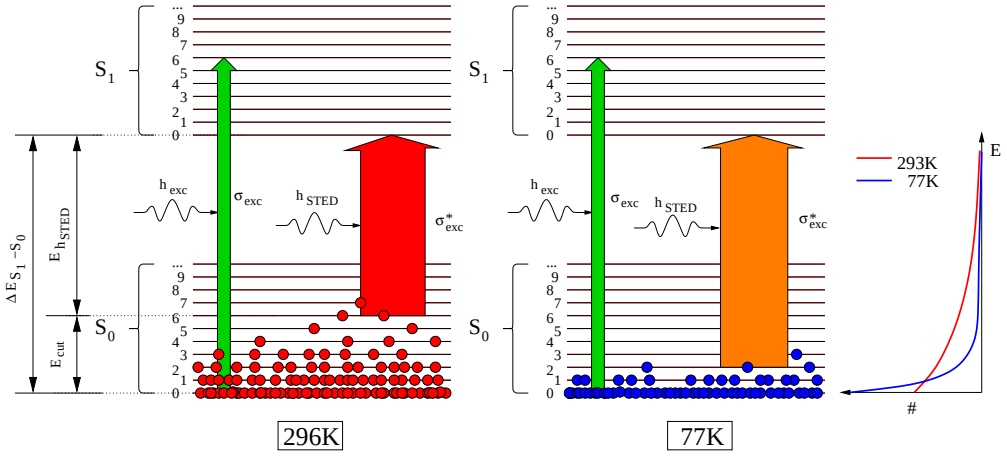

Figure 3.8: Schematic Jablonski diagram considering ground and first excited singlet state of a fluorescent molecule. The occupation density of vibrational states is estimated from expression 3.5 for room temperature (296K, red dots on the left hand side) and liquid nitrogen temperature (77K, blue dots on the right hand side). "'Hot"' vibrational states can be excited to first electronic state S_1 with probability $\sigma^*_{exc} h_{\mathrm{STED}}$. The largest deployable STED wavelength at same anti-Stokes excitation level is a function of energy gap $\Delta E\,(S_1 - S_0)$, E_{cut} and temperature T from expression 3.8.

E_{cut} is given by the integral

$$\#\,(E \geq E_{cut}) = \int_{E_{cut}}^{\infty} dE \exp\left(-\frac{E}{k_B T}\right) \tag{3.6}$$

$$= -k_B T \exp\left(-\frac{E}{k_B T}\right)\Big|_{E_{cut}}^{\infty} \tag{3.7}$$

$$= k_B T \exp\left(-\frac{E_{cut}}{k_B T}\right) \tag{3.8}$$

Since the anti-Stokes excitation cross section is proportional to number of the occupied vibrational states $\#\,(E \geq E_{cut})$, a reduction of temperature will provide an exponential decrease of the anti-Stokes excitation.

Excitation in anti-Stokes regime at different temperatures

The fluorescence excitation and emission spectra are obtained for different temperatures in order to demonstrate the temperature dependency of the excitation cross section in a common fluorescence spectrophotometer. Since the excitation sources attached to a spectrophotometer do not provide the necessary large intensities for STED microscopy, the direct anti-Stokes excitation is measured as function of temperature for the selected STED wavelengths in a custom-built STED microscope.

The Atto532 silica beads are chosen for the appropriate comparability as model sample. For the measurements in a spectrophotometer, a glycerin diluted solution of these beads is cooled inside a custom made flow-through cryostat inset. The excitation and emission spectra are taken at selected temperatures as a function of the wavelength.

The measurements in the STED microscope are carried out at selected STED wavelength as function of the temperature. The value for the anti-Stokes excitation is normalized to the fluorescence level, caused by a common excitation source (532nm, 80MHz laser) with $I_{exc} = 2.2\text{kW/cm}^2$. Therefore two images are taken line by line with the alternating fluorescence excitation with 532nm at 2.2kW/cm^2 and STED wavelength at I_{STED}. This acquisition mode provides two parallel recorded images with different fluorescence origin: (1) excitation with 532nm laser spot and (2) anti-Stokes excitation caused by STED spot. The intensity values of single beads are taken and compared, in a manner that the calculated ratio is plotted as a function of the temperature for selected, measured STED wavelengths. For the wavelengths 560nm, 568nm and 580nm, the triplet depopulation 671nm spot is switched on for both images in order to rule out any triplet population contribution. In case of 605nm measurements, no additional 671nm light is used because no triplet population was observable in the corresponding temperature regime.

Figure 3.9(a) shows the temperature dependence of the fluorescence excitation spectrum. The excitation cross section in the anti-Stokes regime decreases with lower temperatures. Figure 3.9(b) shows the results of the directly obtained anti-Stokes excitation in STED microscopy for the selected wavelengths. The measured ratio $F_{\text{anti-Stokes}}/F$ shows a decrease to zero anti-Stokes excitation contribution with lowering the temperature. The data values are fitted with the function

$$\frac{F_{\text{anti-Stokes}}}{F} = A \cdot k_B T \, \exp\left(-\frac{E_{cut}}{k_B T}\right) + \text{background} \tag{3.9}$$

where A is a proportional factor.

The presented results are conform with the idea of the "'hot"' vibrational states as being the source for the anti-Stokes excitation. Especially the exponential decrease of the anti-Stokes contribution to the fluorescence excitation clearly supports this prediction. The data obtained from these fits are compiled in table 3.1.

The utilization of low temperature in STED microscopy strongly suppress the anti-Stokes excitation. The data for the 560nm STED wavelength show the limit of the liquid nitrogen based cooling. Here the decrease in anti-Stokes excitation stops at the value of 27% at 76K. From the fit function it can be concluded, that the anti-Stokes excitation can be reduced to below 5% by lowering the temperature to 58K at 560nm.

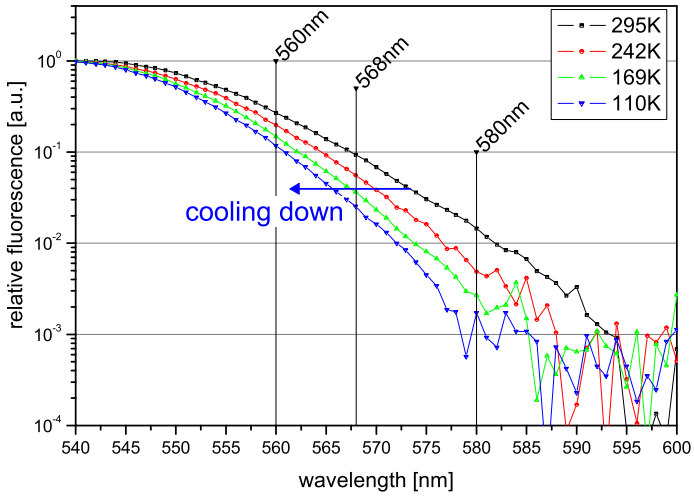

(a) The anti-Stokes regime of excitation spectrum for fluorescent dye Atto532. The excitation cross section as function of wavelength for different temperatures is shown, a reduction for desired STED wavelengths is observed. The excitation value for 580nm STED wavelength is reduced by factor of 14 at 110K.

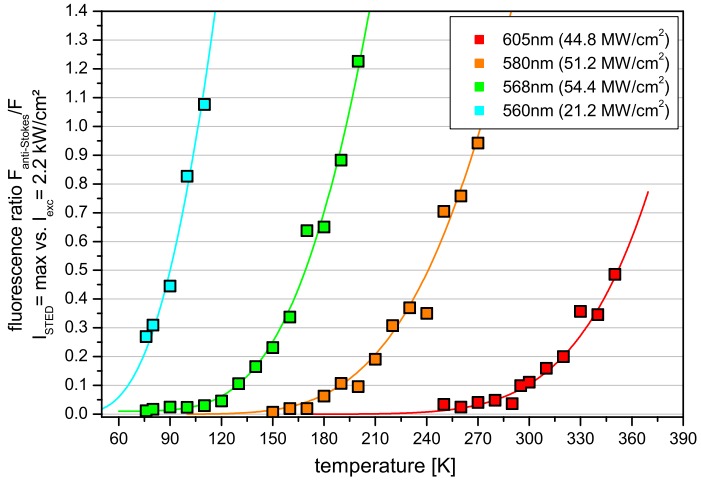

(b) Measurements of the anti Stokes excitation as a function of temperature for the selected STED wavelengths at available intensities. The anti-Stokes excitation ratio decreases exponentially with the lowering of temperature. The data are fitted with Boltzmann distribution model presented in equation 3.8.

Figure 3.9: The compiled results for the anti-Stokes excitation behavior on the temperature and wavelength change.

STED λ	E_{cut}	$F_{anti-Stokes}/F$ at 76K	temperature for 5% excitation
605nm	245 meV	$\ll$1%	280K
580nm	105 meV	$\ll$1%	172K
568nm	68 meV	1 %	115K
560nm	27 meV	27%	58K

Table 3.1: Compiled results from the anti-Stokes excitation measurements.

Benefits to STED microscopy

The application of liquid nitrogen temperatures in the STED microscopy opens the possibility to deploy the STED wavelengths with higher stimulated emission cross section as described in figure 1.4. According to the theory of the STED effect, this will provide higher saturation ratios ξ, and thereby higher resolution enhancement.

3.3 Saturation of stimulated emission depletion

Dependence of fluorescence depletion on STED intensity

The STED microscopy is one of the first experimentally realized and the most developed approaches to subdiffraction light microscopy among the RESOLFT family to date. The resolution enhancement relies on the saturation level of stimulated emisison cross section within the STED concept. According to the theoretical considerations in section 1.3, the saturation characteristic of the fluorescence depletion for utilized pulsed laser sources is described by:

$$F = \exp\left(-\sigma_{\mathrm{STED}} h_{\mathrm{STED}}\right) \tag{3.10}$$

where σ_{STED} is the stimulated emission cross section and h_{STED} is the STED photon flux. The STED photon flux h_{STED} is proportional to the applied laser intensity I. Thus we can define the saturation behavior as a function of the laser intensity as following:

$$F = \exp\left(-\frac{I}{I_{\mathrm{SAT}}}\right) \tag{3.11}$$

The stimulated emission cross section can be then calculated from the reciprocal value $\left(I_{\mathrm{SAT}}\right)^{-1} \sim \sigma_{\mathrm{STED}}$.

The theoretical saturation characteristic from expression 3.11 always shows a complete depletion of the fluorescence. Although, it has been shown for certain experimental conditions that the fluorescence cannot be depleted to zero but remains at a certain residual value [49]. A dependence of the residual fluorescence plateau on the STED pulse width is observed; it is found empirically, that the optimal value lies at about 200-250ps. The utilized pulse width for presented measurements is about 120ps, thus the observed residual fluorescence is expected to originate from that experimental arrangement. Hence the measured data are corrected for the residual fluorescence F_{residual}

$$F\left(I\right) = A\ \exp\left(-\frac{I}{I_{\mathrm{SAT}}}\right) + F_{\mathrm{residual}} \tag{3.12}$$

The measurements of the fluorescence depletion saturation are done at 76K for selected STED wavelengths. As a model sample Atto532 silica beads are used. The fluorescence excitation source is a 532nm, 80MHz laser diode with diffraction limited spot. The stimulated emission is triggered by the OPO system (80MHz), coupled into a 50m long single mode fiber for pulse stretching. The selected STED wavelengths (568nm, 575nm, 580nm and 605nm) do not show any anti-Stokes excitation at 76K (compare with fig. 3.9(b)). The contribution of the triplet population is eliminated by the use of the 671nm diffraction limited spot at maximum available intensity

(∼37MW/cm^2). The spatial alignment of the used PSFs is shown in figure 3.13, the temporal alignment is adjusted for optimal STED efficiency.

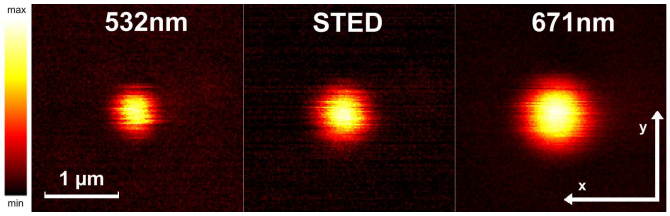

Figure 3.10: The alignment of the PFSs for spectroscopic measurement of STED efficiency.

For obtaining of data, two parallel images are acquired. The first with the illumination of the excitation laser spot (532nm, 80MHz at 2.2kW/cm^2) and the triplet depopulation spot (671nm, CW at ∼37 MW/cm^2), and the second with the excitation and triplet depopulation spots as well as the additional STED spot (80 MHz). The fluorescence intensity for a particular bead is then evaluated from the images with and without STED appliance. The calculated ratio gives the relative fluorescence decrease due to stimulated emission depletion. Acquiring the images with different STED wavelengths and intensities completes the characteristics of the STED behavior at 76K and is presented in figure 3.11.

The measured depletion shows a decay with the applied STED power to the residual fluorescence value about 25% for each particuler STED wavelength. The depletion of the fluorescence F_{STED}/F to a certain value, e.g. 0.5 takes place for lower STED laser power for shorter STED wavelengths.

The data obtained at 76K cannot be fitted with a single exponential decay as a function of the STED laser power. The only sufficient expression to described this data with a model is by use of a stretched exponential decay

$$F\left(I\right) = A\ \exp\left(-\frac{I}{I_{\mathrm{SAT}}}\right)^{\beta} + F_{\mathrm{residual}} \tag{3.13}$$

with $\beta = 0.46(4)$ for every STED wavelength.

Since a particular linear polarization of the excitation and the STED lasers is used for these measurements, a stretched exponential depletion can be explained with a random orientation distribution of the dipoles of the fluorescent markers. At low temperature conditions, the rotation of the dipoles is dramatically suppressed. Thus a dipole with not optimal orientation with respect to the given STED light polarization particularly senses the reduced laser intensity. Hence, differently orientated rigid dipoles contribute with different values for the I_{SAT}. At room temperature, the rotation speed simply smears out the particular contributions, so an averaged value for the I_{SAT}

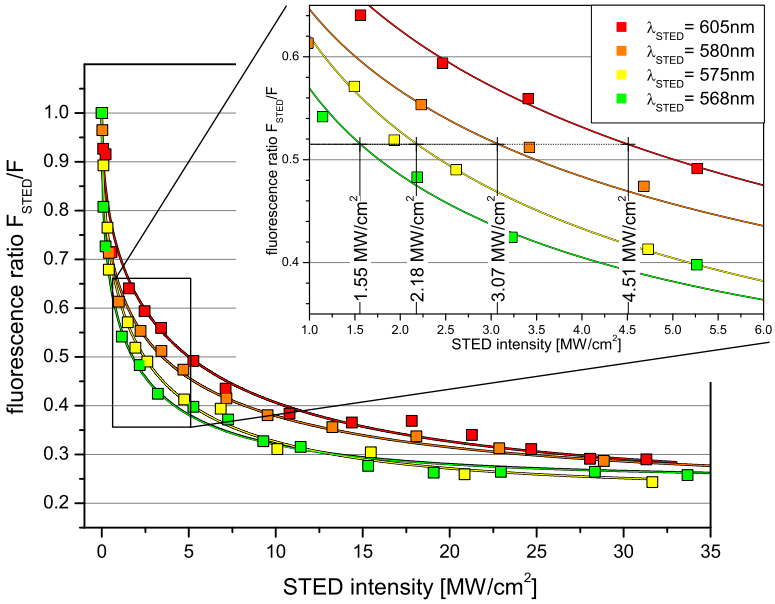

Figure 3.11: Stimulated emission depletion at 76K as a function of STED power for the selected wavelengths (squares), fitted with equation 3.12 (lines). The inset shows the area of interest with the fitted saturation laser intensities I_{SAT}. (sample: Atto532 beads of 65nm in diameter, mounted in glycerin, excited with 532nm 80MHz laser diode, STED with OPO system at 80MHz, triplet depopulation with 671nm CW DPSSL at ~37 MW/cm^2.)

is measured.

Stimulated emission cross section

The key data from the measurements presented in fig. 3.11, the saturation intensities I_{SAT} for selected STED wavelengths are compiled in the table 3.2. Further, the value for stimulated cross sections are calculated by using the relation

$$\sigma_{\mathrm{STED}} = \frac{A_\lambda W_\lambda}{I_{\mathrm{SAT}} \tau_{\mathrm{STED}}} \tag{3.14}$$

where A_λ is the illuminated area, W_λ is the energy of one photon and τ_{STED} is the width of the STED pulse. The measured values I_{STED} are used in expression 1.8 to estimate the relative increase in the resolution with respect to 605nm.

The theoretical expectations on the behavior of the stimulated emission cross sec-

STED wavelength	I_{SAT} [W/cm^2]	$h_{\mathrm{STED}}^{\mathrm{SAT}}$ [cm^{-2}]	σ_{STED} [cm^2]	estimated increase in resolution compared with 605nm
568nm	1.5×10^6	5.8×10^{14}	1.7×10^{-15}	1.7
575nm	2.2×10^6	7.4×10^{14}	1.3×10^{-15}	1.4
580nm	3.1×10^6	10.6×10^{14}	9.4×10^{-16}	1.2
605nm	4.5×10^6	14.5×10^{14}	6.9×10^{-16}	1

Table 3.2: Results from figure 3.11.

tion as function of the wavelength $\sigma_{\mathrm{STED}}(\lambda)$ has been published in literature [35]:

$$\sigma_{\mathrm{STED}}(\lambda) = \frac{\lambda^4 E(\lambda)}{8\pi c n \tau_{fluo}} \tag{3.15}$$

where $E(\lambda)$ is the shape function of the spontaneous fluorescence emission, c is the speed of light, n is the refractive index, and τ_{fluo} is the lifetime of the fluorescent state S_1. The obtained data for the stimulated emission cross sections in table 3.2 (red columns) are compared with the theoretical expectation, calculated according to the expression 3.15 (red line) in figure 3.12.

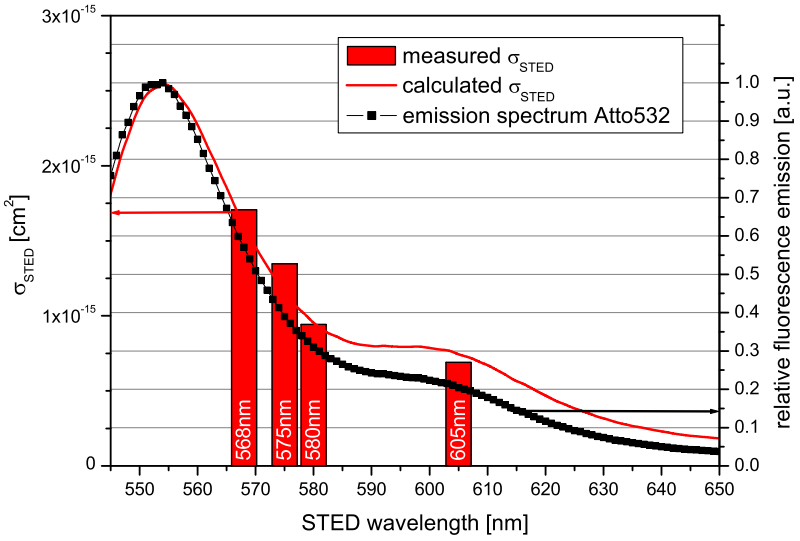

Figure 3.12: Normalized emission spectrum of Atto532 (right ordinate axis) at 76K. Referring to left ordinate axis, the measured (red columns) and the theoretical (red line) values are plotted.

The presented data are in a good agreement with the theoretical considerations.

The stimulated emission cross section is increased by a factor of of 3 at 568nm STED wavelength in respect to 605nm at 76K. The use of this wavelength, which is provided by the introduction of liquid nitrogen temperatures, allows higher saturation ratios at available laser intensities, and thus provides higher resolution enhancement in STED microscopy. The expected resolution enhancement is 1.7 for 568nm with respect to 605nm STED wavelength at same laser intensity I.

3.4 Resolution enhancement

Theoretical considerations

The resolution enhancement in STED microscopy depends on the saturation of the stimulated emission depletion with a modified intensity distribution of the STED PSF, as already described in section 1.3. The expression for the resolution Δr

$$\Delta r = \frac{0.61\lambda}{\mathrm{NA}\sqrt{1+\xi}} \tag{3.16}$$

features two components: (1) a non-linearly saturated stimulated emission depletion, ascribed by the saturation ratio $\xi = I/I_{\mathrm{SAT}}$, and (2) a parabolic intensity shape around the zero with the maximum slope, which provides the square root dependence on the saturation ratio ξ in equation 3.16. The slope of this modified STED intensity has been fully optimized already [31]. Thus, the further resolution increase can be gained by optimization of the saturation ratio ξ. The results of increased stimulated emission cross section, presented in table 3.2, already indicate that the use of shorter STED wavelengths at 76K will provide increased resolution enhancement. In the following section, the resolution enhancement in CryoSTED microscopy is studied.

Resolution at different STED wavelengths

The measurements are carried out on the already presented model sample - Atto532 silica beads of diameter 65nm at 76K. The sample is excited with a 532nm, 80MHz laser diode with a diffraction limited spot. The stimulated emission is depleted by the OPO system (80MHz) tuned to the desired wavelength. For the pulse stretching of the OPO emission from several tens fs to 120ps, a 50m long single mode fiber is used. The zero intensity distribution of the STED PSF is provided by a semi-circular π radiant phase retardation mask. This phase mask provide a resolution enhancement in one lateral direction - the x direction. The temporal alignment of the excitation and the STED pulses is tuned for optimal STED efficiency (see also fig. 2.4). The triplet depopulation laser source (671nm, CW) is deployed at maximum available intensity ($\sim$37MW/cm^2) for these measurements intentionally to eliminate any triplet influence. The spatial alignment of the PSFs used is shown in figure 3.13.

For the characterization of the dependence of the resolution ability on the STED power, parallel confocal image (excitation and triplet depopulation illumination) and STED image (excitation, triplet depopulation and STED illumination) are recorded for several STED laser intensities. Then approximately 50 particular and distinguishable beads are analyzed for the full width at half maximum (FWHM) intensity, which is an indicator for the resolution ability of the microscope. A more detailed description

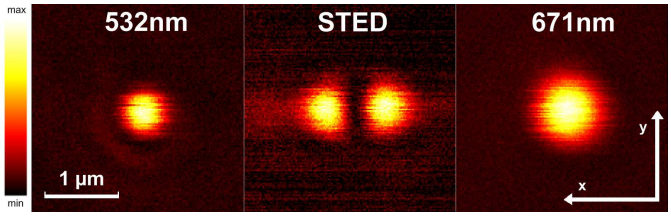

Figure 3.13: The alignment of the PSFs for resolution enhancement in x direction.

STED wavelength [nm]	FWHM at 20MW/cm^2 [nm]	enhancement factor at 20MW/cm^2	rel. increase in resolution compared to 605nm	$I_{1/2\mathrm{FWHM}}$ [W/cm^2]
568	142	3.3	1.6	6.4×10^6
580	212	2.2	1.1	15.6×10^6
605	222	2.1	1	17.8×10^6

Table 3.3: Compiled key data for the STED resolution at different wavelengths.

of the analysis can be found in appendix A. The figures 3.14(a) and 3.14(b) show details of a 10×10 μm^2 image; on the left hand side, the STED image unveils a resolution enhancement in the x direction, compared to the confocal image at the same position on the right hand side. The averaged line profile in the x direction over a single bead, marked with the white circle in figure 3.14(a), is shown in figure 3.14(c) for comparison between the confocal image (black squares) and the STED image (red squares). While the confocal FWHM is 472nm, which is in good agreement with the Abbe formula for the utilized $\mathrm{NA} = 0.7$, the STED FWHM is 128nm. This provides a resolution enhancement of 3.7. The example in figure 3.14(b) even unveils two neighboring fluorescent beads in x direction. The distance between these beads is 389nm, and thus cannot be resolved by the confocal PSF.

Such images are taken at selected STED wavelengths (568nm, 580nm and 605nm), each at varying intensities. The averaged FWHMs are obtained for every image by accounting at least 50 beads for a particular STED intensity. These FWHMs are plotted in figure 3.15 against the logarithmically scaled intensity. The values for the particular STED wavelengths are fitted with the equation 3.16.

The starting value of the FWHM is around 468nm, this value is conform with the confocal resolution. With increasing STED intensity I, the value of the obtained FWHM decreases with different slopes for particular wavelengths. An indicator for this decrease rate due to intensity is the value $I_{0.5\times\mathrm{FWHM}}$, this value is reached when the resolution is increased by factor of 2. The fastest decrease is observed for the wavelength $\lambda_{\mathrm{STED}} = 568$nm, the slowest for the $\lambda_{\mathrm{STED}} = 605$nm. The key data are compiled in the table 3.3

The utilization of STED wavelength with higher stimulated emission cross section at

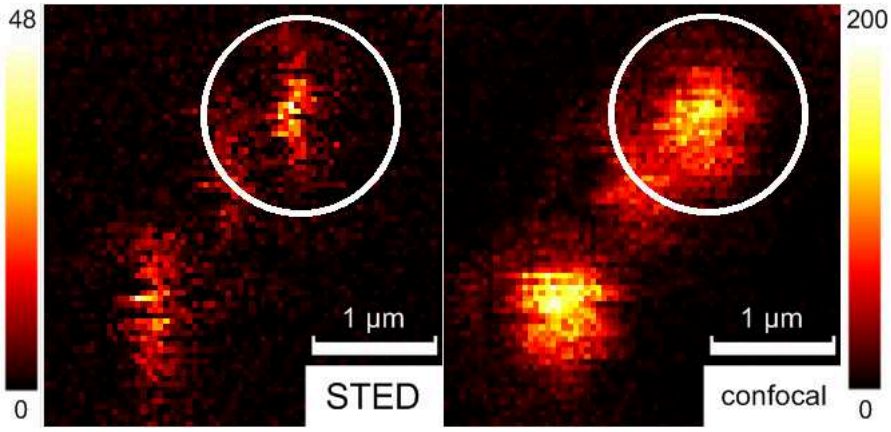

(a) Detail of a STED and the corresponding confocal image from Atto532 beads. The STED image shows a narrowing of fluorescence intensity distribution in x direction.

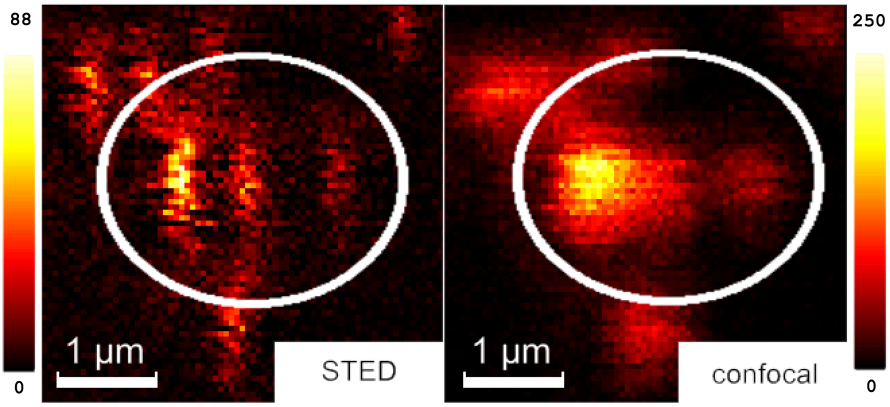

(b) Resolving of two neighboring beads in x direction by the CryoSTED microscopy.

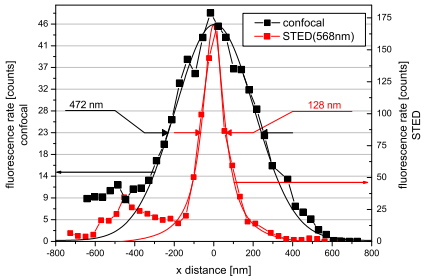

(c) An averaged profile in x direction taken from the image 3.14(a) inside the white circle with confocal FWHM = 472nm and STED FWHM = 128nm.

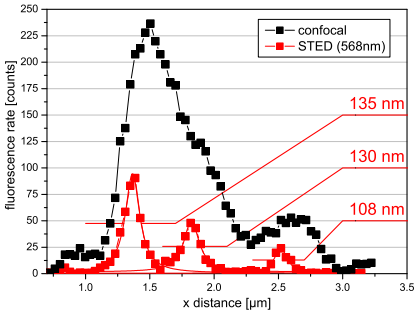

(d) An averaged x-line profile inside the white ellipse in figure 3.14(b); STED picture unveils two neighboring beads, which are undistinguishable in the corresponding confocal image.

Figure 3.14: Details of examplary confocal and STED images, recorded at 76K. Deployed STED wavelength is 568nm at 25.6MW/cm^2.

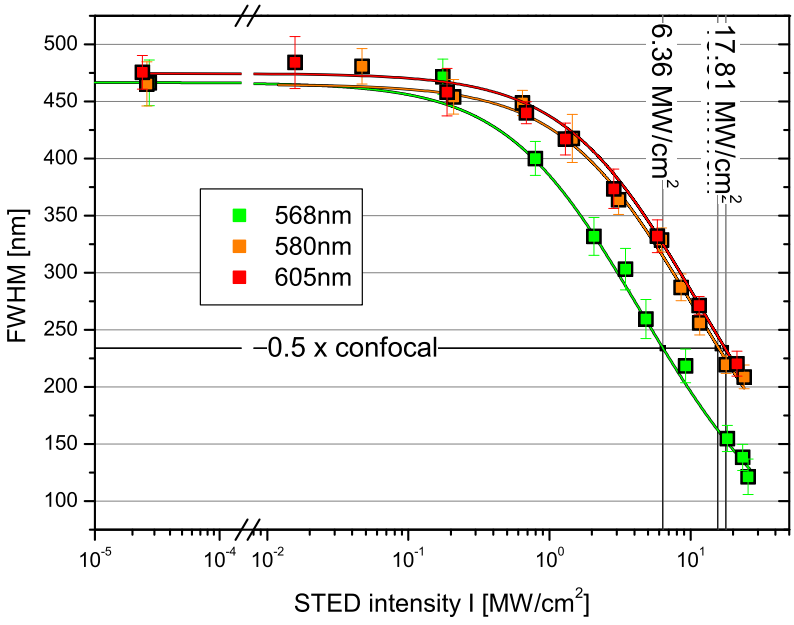

Figure 3.15: Dependence of the FWHM on different STED wavelengths and STED laser intensities.

76K provides a greater resolution enhancement within the STED microscopy. This is in agreement with the theoretical expectations, since the resolution enhancement relys on the saturation ratio $\xi = I/I_{\mathrm{SAT}}$. The relative increase in the resolution enhancement from table 3.3 are in full agreement with the values from table 3.2, where the measured values for the stimulated emission cross section are used for the estimation.

The introduction of CryoSTED microscopy allows the deployment of STED wavelengths with larger stimulated emission cross sections due to the absent anti-Stokes excitation at 76K. Thus higher STED saturation ratios ξ are available which provide higher resolution enhancement with respect to the STED microscopy at room temperature. The negative influence of the triplet population at 76K is eliminated by the additional use of a triplet depopulating laser.

3.5 Influence of the triplet population on resolution

The influence of the triplet population on the fluorescence brightness was already discussed in detail in section 3.1, while the issue of the STED efficiency shall be dealt within this section. In the previously presented measurements, the influence of the triplet state population was eliminated by utilization of the 671nm laser source, now we shall discuss the influence of the high triplet population on the resolution in CryoSTED microscopy.

The experimental conditions are chosen in same manner, like for the resolution enhancement measurements. The only difference is that now the 671nm laser spot illumination is chopped in between the images recorded parallel. Thereby the first image contains the fluorescence signal after illumination with the excitation spot (532nm, 80MHz) and the modified STED spot (605nm, 80MHz) with an applied semi-circular phase mask at varying intensities, while the second image is additionally illuminated by the triplet depopulation spot (671nm, CW). Figure 3.16 shows the xy intensity distributions of the PSFs, measure on scattering gold spheres.

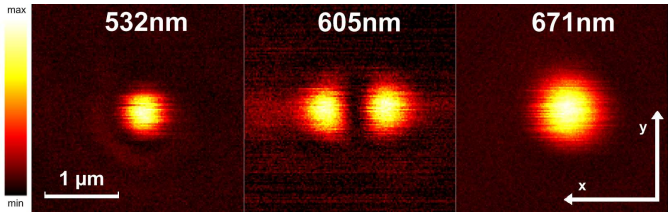

Figure 3.16: The alignment of the PSFs for resolution enhancement in x direction.

Figure 3.17 shows the parallel recorded images of the fluorescent specimen with 671nm illumination (left hand side) and without (right hand side) for different STED intensities. While the image in the first row with 671nm illumination shows a good signal to noise ratio (268 counts in maximum to 4 counts as background), the image without the 671nm triplet depopulation illumination is darker (75 counts in maximum to 4 counts as background). With increasing the STED intensity, the difference in fluorescence brightness becomes smaller between the images with and without the 671nm illumination.

The effect on the resolution enhancement is shown in figure 3.18, where the FWHM of the beads is plotted as function of the STED intensity. The as black squares marked values show the already observed behavior of the resolution enhancement for the STED wavelength of 605nm, the FWHM is continuously reduced and follows the theoretical expression 3.16. The behavior of the resolution without the additional 671nm illumination (red squares) shows a more complex behavior with the increasing STED intensity. First, the averaged FWHM increases to the value of 580nm, which

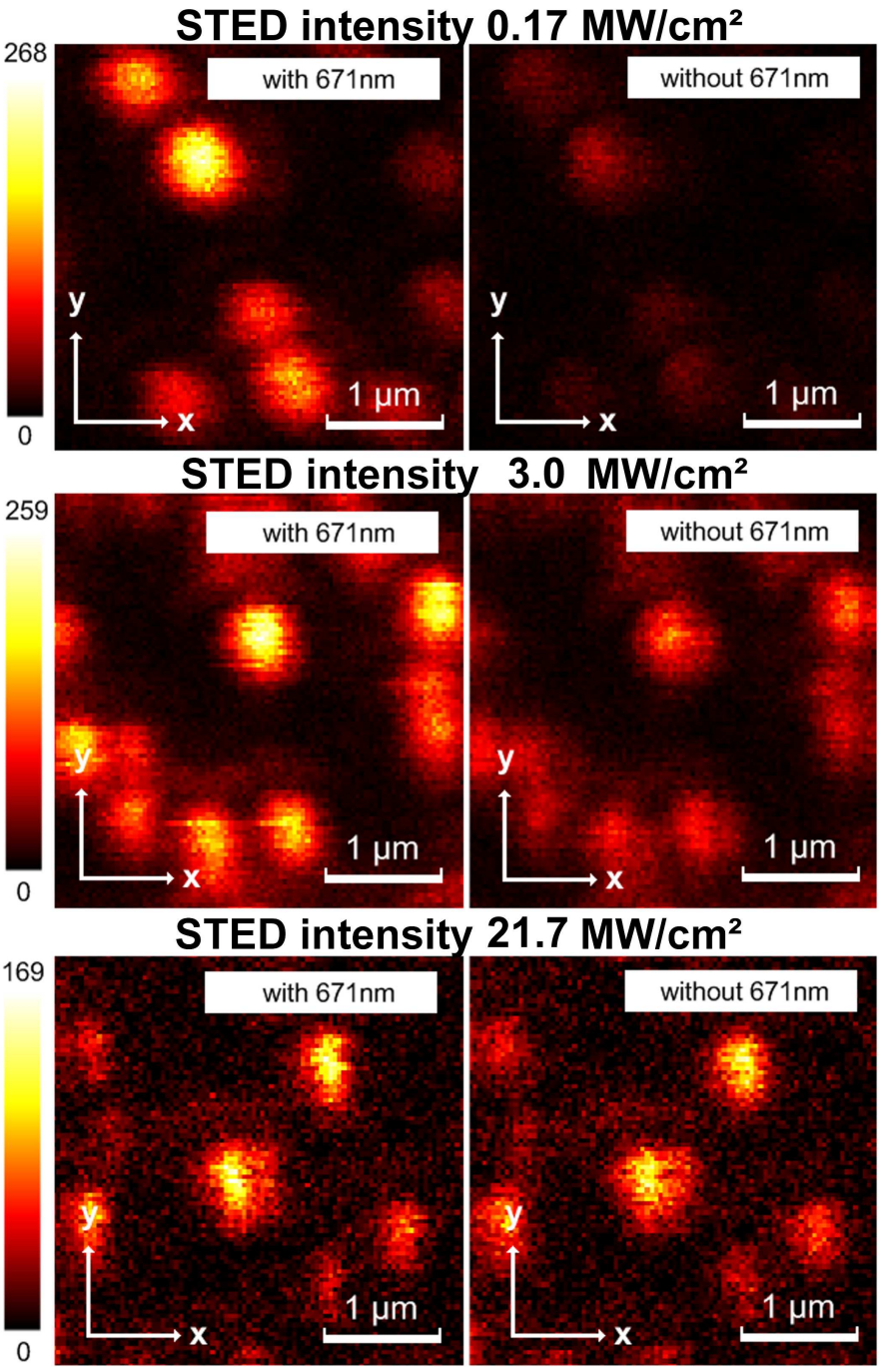

Figure 3.17: Images taken with additional (left hand side) and without (right hand side) the additional triplet depopulation illumination for three different STED intensities, $I_{\mathrm{STED}} = 0.17$ MW/cm^2 for first row, 3.0 MW/cm^2 in second row and 21.7 MW/cm^2 in last row.

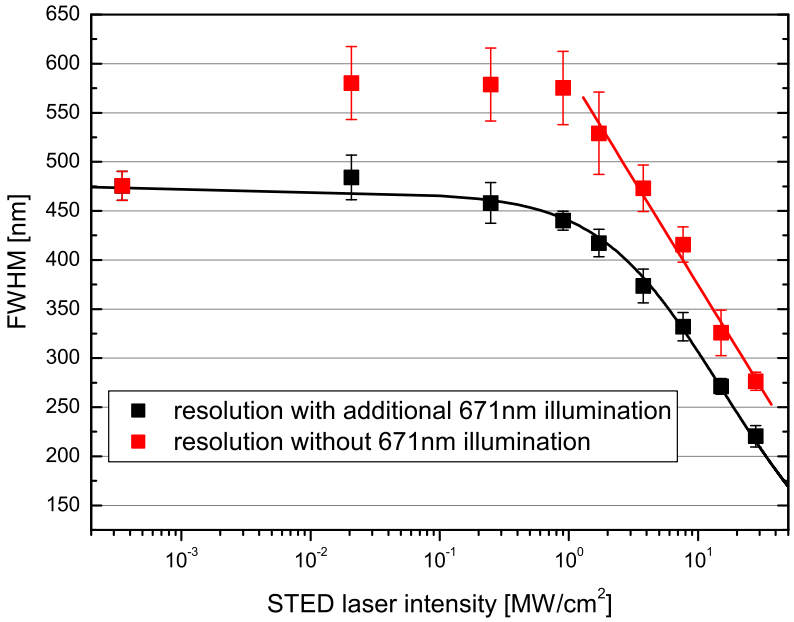

Figure 3.18: Influence of the triplet population on the CryoSTED resolution. Comparison between (1) the triplet depopulation is activated (black squares) and (2) the triplet depopulation is deactivated (red squares).

is 1.3 times higher than the initial confocal FWHM of 472nm, with a subsequent decrease. The values of the FWHM, obtained without additional 671nm laser illumination (red squares) lag those obtained with the additional 671nm laser illumination (black squares).

While the resolution dependence with the additional triplet depopulation (black squares) is in good agreement with the theoretical expectations, the interpretation of the measurement without the additional triplet depopulation laser spot is more complicated. In section 3.1 it has been shown that the molecules trapped in triplet can absorb a STED photon and thereby cross to the singlet state. This rate is competing with the stimulated emission depletion. For small STED intensities, in this case under 1 MW/cm^2, the triplet depopulation due to STED intensity is more pronounced than the stimulated emission. Since the main STED intensity is applied in the outer region of the confocal PSF due to the desired intensity distribution with a zero (compare with figure 3.16), the fluorescence brightness is enhanced in these areas and the effective PSF is broadened. Thus, the resolution ability decreases to the obtained FWHM value of 580nm. Now, with further increasing of the STED intensity, the simulated emission becomes more prominent, because the triplet state is already depopulated. So, a

present triplet population introduces a competing rate to the stimulated emission, and thus reduces the STED efficiency. The resolution enhancement is pronouncedly reduced by nearly 65nm at the maximum available STED intensity without the triplet depopulation.

The presented measurements once again highlight the importance of triplet depopulation in CryoSTED microscopy. The results clearly show that the utilization of an additional triplet depopulating laser source provides higher fluorescence yield as well as an optimal STED efficiency, and thus optimal resolution.

3.6 Bleaching properties at low temperatures

Bleaching in STED microscopy

The resolution enhancement within STED microscopy relies besides the saturation ratio ξ of the stimulated emission depletion also on the fatigue resistance of the molecules, because bleached molecules cannot contribute to the fluorescence cycle anymore. Unfortunately, the STED concept demands much higher fatigue resistivity of the molecules than conventional fluorescence microscopy. Only the molecules in close vicinity to the zero of a STED PSF contribute to the fluorescence brightness, while the molecules in the outer region of the excitation spot are excited and subsequently de-excited again without any contribution to the fluorescence. Thus fluorescent markers undergo much more excitation – de-excitation cycles and thereby they suffer from higher bleaching probability.

The causes for the bleaching are manifold because there are many different ways to destroy the fluorescent core, the π-electron configuration, e.g. by chemical reactions or structural changes. The most prominent way for bleaching is a chemical reaction of the excited fluorescent marker with a highly reactive molecule, such as oxygen. The dependence of bleaching probability on the triplet population and the oxygen concentration at room temperature has been studied before [36]. The contribution of highly excited energetic states $\mathrm{S_N}, \mathrm{T_N}$ to the bleaching has also been discussed in the context of highly increase reactivity, and thereby bleaching probability [41], especially due to excitation into $\mathrm{S_N}, \mathrm{T_N}$ states by the STED light [50, 51].

The average velocity of chemical reactions relies on the diffusion time of highly reactive molecules, e.g. oxygen. The cooling of the sample to 76K strongly reduces the diffusion time, and thus provides higher stability for the fluorescent molecules in the $\mathrm{S_N}, \mathrm{T_N}$ states. The velocity rate of a chemical reaction itself is exponentially suppressed by the reduction of temperature as described by Arrhenius law (see page 11). Both, the reduced diffusion constant and the rate for a chemical reaction, enhance the fatigue resistivity at 76K, and thereby allow an application of higher laser intensities in CryoSTED microscopy.

The bleaching probability is measured for Atto532 beads, the excitation and STED parameters are the same as presented in section 3.5. Now, ten STED images are recorded consequently at the same position at room temperature (293K) and low temperature (76K). The evolution of the averaged intensity as well as the FWHM of the beads are evaluated as function of the image number. Since hardly any triplet population can be observed at room temperature, the application of the 671nm laser spot is not necessary at 293K. At 76K the sample is illuminated with the 671nm laser spot at maximum available intensity ($\sim$37MW/cm^2) in order to eliminate any triplet population influence.

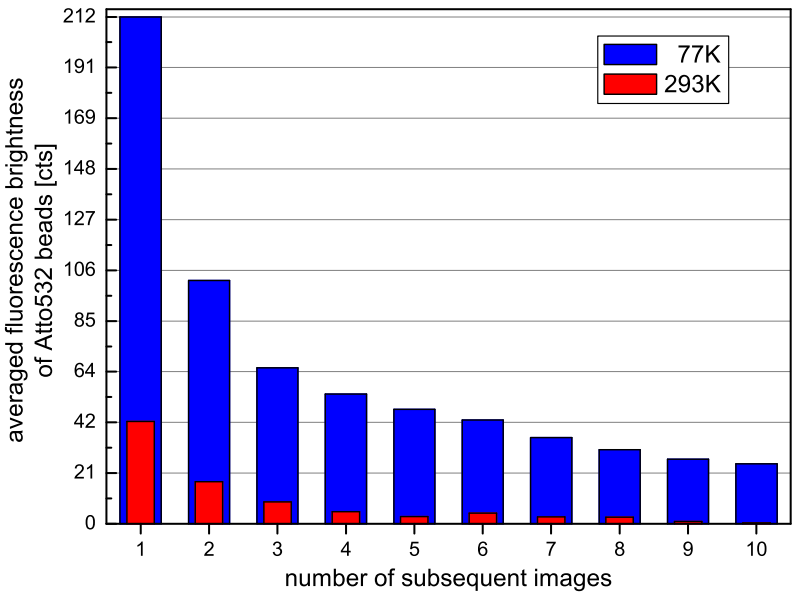

Figure 3.19: Averaged brightness of fluorescent Atto532 beads as function of number of images at 76K (blue columns) and 293K (red columns).

Figure 3.19 shows the evaluation for the fluorescence brightness development at 76K (blue columns) and at 293K (red columns). In case of room temperature, the fluorescence decreases from its initial value of 43 counts down to nearly 4 counts in the fourth image. The background noise in the picture is below 2 counts. The FWHM evaluation is possible for only the first three images, the values show no dependence on the number of image and stay at around 254nm FWHM within an error of 1nm. The evaluation of the FWHM for the images 4-10 is not possible due to poor signal to noise ratio.

The situation at 76K is different, the averaged fluorescence brightness in the first image is 212 counts. The brightness decreases subsequently and is 25 counts in the tenth image. The background noise is again below 2 counts. The evaluated FWHM shows no dependence on the number of images and stays stable for all 10 images around the value of 254nm FWHM within an error of 4nm.

On one hand, the absolute brightness value is five times higher in the initial STED image at 76K with respect to room temperature. In the tenth image the difference is even 63. This brightness increase can stem from several causes:

- reduction of the temperature reduces the rate of the internal conversion and thereby increases the fluorescence quantum yield

- the introduction of complete triplet depopulation due to additional 671nm laser spot illumination also increases the fluorescence yield by reducing the dark time, while the molecules stay in the triplet state
- higher stability in terms of fatigue resistivity increases the total number of fluorescence photons

Usually, Atto532 has a fluorescence quantum yield of ∼90% in water, but the change of the environment from an aqueous solution to a rigid silica matrix can cause a reduction of the quantum yield. The value for the fluorescence quantum yield in these silica beads as well as the quantitative triplet population of Atto532 at room temperature are hardly experimentally accessible. Thus a quantitative assignment of the relative brightness increase at 76K is not possible without further experiments. However, the fact of the enhanced signal to noise ratio is a benefit itself to STED microscopy .

The relative behavior of the bleaching can be described by double exponential decay in the number of images n with a fast and a slow decay constants, η_{fast} and η_{slow}, respectively:

$$F(n) = A_{\text{fast}} \exp\left(-\frac{n}{\eta_{\text{fast}}}\right) + A_{\text{slow}} \exp\left(-\frac{n}{\eta_{\text{slow}}}\right) \tag{3.17}$$

The fitted decays from experimentally measured values are compared in following table

temperature	η_{fast}	η_{slow}
76K	0.71	8.1
293K	0.67	3.1

The double exponential decay usually explains two different populations, which show different bleaching behavior. The brightness decrease in figure 3.19 indicates a fast and a slow bleaching population of the fluorescent molecules. While the fast decay constant η_{fast} is comparable for both temperatures, there is a huge difference in the slow brightness decay η_{slow}. This population is 2.6 times more stable at 76K compared with 293K.

Especially the longer slow bleaching decay τ_{slow} indicates high stability of the fluorescent markers at 76K in terms of photo-bleaching. The increased fluorescence brightness at low temperatures increases the signal to noise ratio in STED microscopy. Both, the higher photo-bleaching stability and the enhanced signal to noise ratio are advantageous to CryoSTED microscopy.

Chapter 4

Conclusion and outlook

4.1 Advantages of the CryoSTED microscopy

This work introduces the STED microscopy at cryogenic temperatures (CryoSTED) as an improvement of the present day STED microscopy. Performing high-resolution STED fluorescence imaging at liquid nitrogen temperatures holds several exceptional advantages.

Elimination of the anti-Stokes excitation

The anti-Stokes excitation has prevented the use of STED wavelengths with larger stimulated emission cross sections to date. This work has shown an exponential decrease of the anti-Stokes excitation with lowered temperature. These measurements clearly indicated that the hot tail of the Boltzmann distribution of the vibrational excited states is responsible for the direct fluorescence excitation caused by the STED light at room temperature. The lowering of the temperature reduces the population of the higher excited vibrational states, and thereby reduces the fluorescence excitation at high STED intensities.

The successful suppression of the anti-Stokes excitation at liquid nitrogen temperature allows the use of more blue-shifted STED wavelengths with larger stimulated emission cross sections, and thereby higher STED efficiency. An increase in the STED efficiency by a factor of 3.7 compared with room temperature has been proved. This leads to an resolution enhancement by a factor of 1.6.

The presented resolution enhancement is achieved with a STED wavelength of 66% STED efficiency with respect to the fluorescence emission maximum. The further improvement can thus be achieved by the use of even lower temperatures, which requires an utilization of liquid helium. The use of STED wavelengths which are the same as

the maximum fluorescence emission wavelengths shall provide an improvement of factor 2.2 in the resolving power with respect to the present day STED microscopy.

Triplet depopulation

At liquid nitrogen temperature, the fluorescence microscopy suffers to large dark triplet population of the fluorescent markers. Because the relaxation rate of the triplet state into the singlet ground state is reduced by several orders of magnitude at 76K, a relative triplet population of between 80% and 90% has been observed. During this work, an efficient light driven triplet depopulation technique has been developed. The use of an additional laser spot with an appropriate wavelength provides a complete depopulation of the dark triplet state, and thereby improves the fluorescence brightness by upto 7-8 times, and thereby enhances the signal to noise ratio.

A further advantage over room temperature microscopy lies in the complete control of the triplet population. Since the light-driven triplet depopulation at room temperature is hampered by photo-bleaching, the triplet state can only be depopulated by thermal relaxation, and therefore the use of low repetition rate laser sources is necessary. This technique (D-REX, [19]) brings along very long acquisition times and a poor signal to noise ratio as compared to the CryoSTED microscopy.

Reduced photo-bleaching probability

The use of liquid nitrogen has strongly reduced the photo-bleaching probability – a major problem in room temperature STED microscopy. Exemplary data for an organic dye indicates a 2.6 times larger photo-stability in CryoSTED microscopy.

The contribution of the triplet state related photo-bleaching can be excluded at 76K due to the continuous triplet depopulation with an additional wavelength. Thus the photo-bleaching reactions most probably take place from the singlet excited states, and low temperature condition suppresses the probability of chemical reaction due to the Arrhenius law. This photo-stability will most likely allow larger applicable laser intensities to the fluorescent specimen, and thereby increase the saturation ratio ξ additionally to the enhancement due to the stimulated emission cross section.

Technical restrictions on the numerical aperture

The introduction of the low temperatures necessitates vacuum technology to shield the sample thermally from the environment. An appropriate way is to use a vacuum chamber for the sample and to use an objective lens placed outside this chamber. This necessitates an air objective lens with a long working distance, which technically restricts the numerical aperture to the maximum value of 0.7 to date. Such small

numerical aperture provides a smaller resolving power with respect to the normally used NA of 1.4 in the STED microscopy at room temperature. However, this technical restriction has to be solved within the next design of CryoSTED microscope.

The role of numerical aperture within the RESOLFT concept

To discuss the impact of the presented topics on the resolution in STED microscopy, its mathematical is first deduced. According to the equation 1.8, the resolution of a STED microscope for large intensities is given by:

$$\Delta r \cong \frac{0.61\lambda}{\mathrm{NA}\sqrt{\frac{I}{I_{\mathrm{SAT}}}}} \tag{4.1}$$

The laser intensity I is given by

$$I = \frac{P}{A_\lambda} \tag{4.2}$$

Here P is the laser power within the focused spot in watt [W] and $A_\lambda = 0.25\pi\,(\mathrm{FWHM})^2$ is the area of the focused light in square centimeters [cm^2], and $\mathrm{FWHM} = 0.61\lambda/NA$ is the full width at half maximum of the diffraction limited focused spot. Thus the resolution is given by:

$$\Delta r = \frac{0.61\lambda}{\mathrm{NA}\sqrt{\frac{4P}{\pi(\mathrm{FWHM})^2 I_{\mathrm{SAT}}}}} \tag{4.3}$$

$$= \frac{1}{2\mathrm{NA}^2\sqrt{\frac{P}{\pi I_{\mathrm{SAT}}}}} \tag{4.4}$$

The introduction of CryoSTED microscopy has enhanced the resolution by a decrease of the saturation intensity I_{SAT} due to larger stimulated emission cross section, and shall allow the use of higher laser power P due to enhanced photo-stability. Since the most prominent dependence of the resolution is on the numerical aperture, the further improvement necessitate the use of higher numerical apertures within the CryoSTED microscopy.

4.2 The future development of CryoSTED microscopy

Use of higher NA

In this work, an air objective lens with a NA of 0.7 was used due to the need for large working distance. The use of larger NA requires a re-design of the cryostat, where an objective lens can be placed inside the vacuum chamber. This concept shall allow the

use of short working distances, and thereby NA values of upto 0.9. An other interesting concept would be the use of solid immersion lenses [52], but it necessitates a high technical effort. Here, the numerical aperture depends on the choice of the immersion medium and provide the NA values of upto 2.0 [53].

The table 4.1 shows the estimated resolutions for different scenarios. The estimation is based upon the measured STED efficiency for an organic dye, Atto532 at 76K and upon the equation 4.4. As STED laser sources two commercially available systems are presented, (1) an OPO at 80MHz (APE, Germany) and (2) an OPA at 350kHz (Coherent, USA) with 8 times higher peak power compared to the OPO system. The

NA	0.7	0.9	1.4
FWHM with OPO (80MHz)	120nm	57nm	15nm
FWHM with OPA (350kHz)	43nm	20nm	6nm

Table 4.1: Estimation for the obtainable resolution based upon measured STED efficiency for an organic dye (Atto532) and upon equation 4.4.

presented estimation confirm the huge potential of CryoSTED microscopy.

Applications of CryoSTED microscopy

Besides the ability to resolve even the smallest structure inside a cell, e.g. ribosomes, where the proteins are assembled, the main advantage of such a small effective PSF (Δr < 10nm) is the high precision for size measurement of structures inside cells. Such small sizes of the effective PSF is even below the thickness of the double layered membrane. Therefore with specific labeling, the inner and outer membranes should become distinguishable with such high precision.

The resolution capability of below 10nm comes into the range of an electron microscope and could easily compete with this technique due to the advantages of the fluorescence microscopy, such as specific labeling, high fluorescence contrast and the ease of the 3D structure observation.

Appendix A

Image processing

Software time gating

Due to the refractive index mismatch between glycerin and glass, a scattered light from the laser sources was additionally detected with the confocal APD. Since the scattered and the fluorescence light show different temporal characteristics, these can be separated with the TCSPC measurement mode of the SPC730 card (Becker & Hickel, Germany). Therefore the images are recorded in a mode, where the arrival time histogram is obtained for each pixel as shown in figure A.1. The arrival time histogram (upper graph in fig. A.1(b)) is analyzed for scattering signal, and if some appears, it can be eliminated by deleting the referring time bins (as indicated in lower graph of fig. A.1(b)).

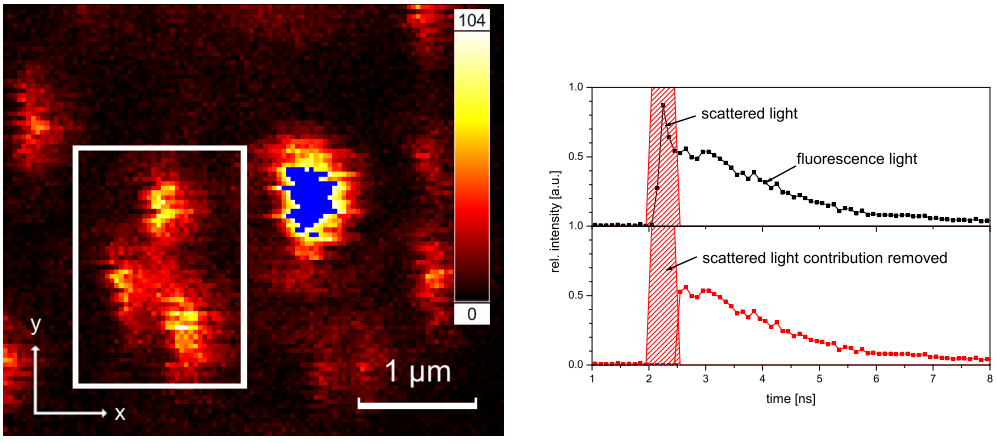

(a) Raw picture

(b) Time of flight histogram

Figure A.1: Appeared scattering signal of pulsed laser in raw pictures can be removed from time of flight histogram taken with SPC730 photon counting card.

Deconvolution of images

The saturation characteristics, presented in section 3.3, have shown a residual fluorescence of around 25% during the depletion. Thus the sub-diffraction efective PSF consists out of a confocal and a sub-diffraction contribution. This is shown in figure A.2. The fig. A.2(a) shows a raw STED image of Ato532 silica beads. A line profile in the x direction shows the contribution of the confocal resolution (gaussian fit with FWHM=484nm) and of the STED enhanced resolution (Lorential fit with FWHM=120nm). To obtain the resolution enhancement due to STED, the images have to be deconvoled. The appropriate way to do this is to subtract a certain fraction of the parallel recorded confocal image from the STED image [54].

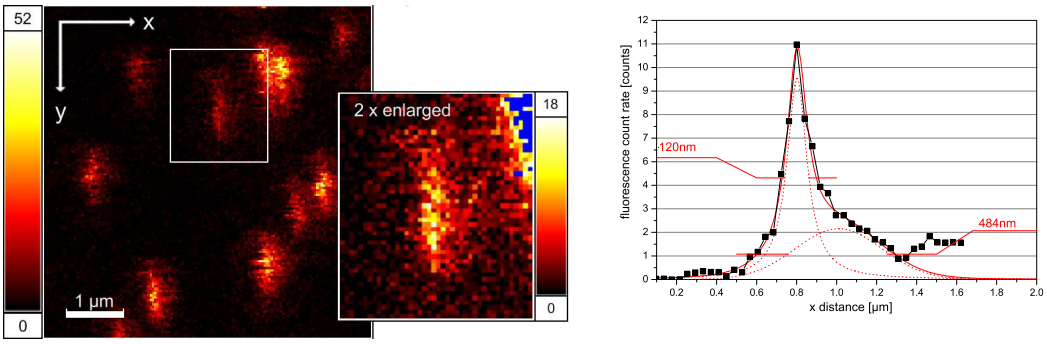

(a) STED picture taken at 76K with $\lambda = 568$nm. Exemplary bead is enlarged by factor of 2.

(b) Averaged line scan (21 contributing lines) through enlarged bead (inset A.2(a))

Figure A.2: Confocal and STED contributions in CryoSTED microscope due to non-zero fluorescence depletion.

The nature of liquid nitrogen, especially its wave-like evaporation, introduces vibrations to the fluorescence images at 76K. A technical solution requires a re-design of the cryostat system. For obtaining the FWHM, the x profiles over each bead have to be un-waggled first. This is provided by a computer program, which maximizes the correlation signal of the neighboring x profiles [55]. This procedure is only applied for the calculation of the FWHM, so no un-waggled images are shown in this thesis.

Acknowledgement

In this place, I would like to thank all the people who has supported me during the CryoSTED project:

Prof. Stefan Hell for the possibility to work on such an interesting topic, the STED microscopy. He always had an open ear and put a lot of new ideas into this project.

Prof. Christoph Cremer for his interest and being the second referee of this thesis.

Dr. Christian Eggeling for his kind advice, the daily discussions, a lot of good ideas during this thesis and proof-reading of the manuscript. His expertise benefits a lot to the CryoSTED project.

Dr. Chaitanya Ullal, Dr. Miriam Schwentker, Dr. Jan Keller and Jaydev Jethwa for proof-reading of the manuscript.

Dr. Mariano Bossi for preparing the fluorescent silica beads and sharing his knowledge about the fluorescent dyes.

The staff of the mechanical workshop for many useful devices, the CryoSTED project benefits a lot from their experience in mechanical precision constructions.

Dr. Andreas Schönle for his support with all the new drivers within the imspector measurement software.

Dr. Jan Keller for providing the small evaluation programs, such as PSF_calc and unwaggle.

Jaydev Jethwa for sharing his wisdom, especially about the laser technology.

Donald Ouw for Cary Eclipse measurements and nice custom-build low temperature gadgets.

Harald Meyer for the help with computer parts and electrical wiring.

The staff of the optical shop for the preparation of phase masks.

Dr. Norbert Quaas, who has accompanied the project during the very initial steps.

Lab and office colleagues, they provided a very nice working environment.

My friends and colleagues, with whom I had very nice time in the last years.

My family, who encouraged and supported me over all the years.

Bibliography

[1] Robert Hooke. *Micrographia, or Some physiological descriptions of minute bodies made by magnifying glasses*. J. Martyn and J. Allestry, London, first edition, 1665.

[2] Ernst Abbe. Beiträge zur Theorie des Mikroskops und der mikroskopischen Wahrnehmung. *Archiv für Mikroskopische Anatomie*, 9:413–420, 1873.

[3] M. Knoll and E. Ruska. Das Elektronenmikroskop. *Zeitschrift für Physik*, 78:318–339, 1932.

[4] J.L. Farrant. Wavelengths suitable for x-ray microscopy of biological specimen. *J. Appl. Phys.*, 21:63f, 1950.

[5] V.E. Cossette and W.C. Nixon. The x-ray shadow microscope. *Nature*, 168:24f, 1951.

[6] P.A. Temple. Total internal reflection microscopy: a surface inspection technique. *Applied Optics*, 10:2656ff, 1981.

[7] D.W. Pohl, W. Denk and M. Lanz. Optical stethoscopy: Image recording with resolution $\lambda/20$. *Appl. Phys. Lett.*, 44:651ff, 1984.

[8] M. Osborn, W.W. Franke and K. Weber. Visualization of a system of filaments 7-10nm thick in cultured cells of an epithelioid line (PtK2) by immunofluorescence microscopy. *PNAS*, 74:2490–2494, 1977.

[9] M. Chalfie, Y. Tu, G. Euskirchen, W.W. Ward and D.C. Prasher. The green fluorescent protein as a marker for gene expression. *Science*, 263:802–805, 1994.

[10] Jan Slavik. *Fluorescence microscopy and fluorescent probes*. Springer, 1996.

[11] M. Minsky. Microscopy apparatus. US Patent 3,013,467, 1961.

[12] S.W. Hell. Toward fluorescence nanoscopy. *Nature Biotechnology*, 21:1347–1355, 2003.

[13] E. Betzig G.H. Patterson, R. Sougrat, O.W. Lindwasser, S. Olenych, J.S. Bonifacino, M.W. Davidson, J.Lippinscott-Schwartz and H.F. Hess. Imaging introcellular fluorescent proteins at nanometer scale. *Science*, 313:1642–1645, 2006.

[14] S.T. Hess, Thanu P.K. Girirajan and M.D. Mason. Ultra-high resolution imaging by fluorescent photoactivation localization microscopy (fpalm). *Biophysical Journal*, 91:4258–4272, 2006.

[15] S. Bretschneider, C. Eggeling and S.W. Hell. Breaking the diffraction barrier in fluorescence microscopy by optical shelving. *Phys. Rev. Lett.*, 98:218103, 2007.

[16] M.G.L. Gustafsson. Nonlinear structured-illumination microscopy - wide-field fluorescence imaging with theoretically unlimited resolution. *PNAS*, 102:13081–13086, 2005.

[17] M.A. Schwentker, H. Bock, M. Hofmann, S. Jakobs, J. Bewersdorf, C. Eggeling and S.W. Hell. Wide-field subdiffraction RESOLFT microscopy using fluorescent protein photoswitching. *Microscopy research and technique*, 70:269–280, 2007.

[18] M. Bossi, J. Fölling, M. Dyba, V. Westphal and S.W. Hell. Breaking the diffraction resolution barrier in far-field microscopy by molecular optical bistability. *New journal of physics*, 8, 2006.

[19] G. Donnert, J. Keller, R. Medda, M. A. Andrei, S. O. Rizzoli, R. Lührmann, R. Jahn, C. Eggeling and S. W. Hell. Macromolecular-scale resolution in biological fluorescence microscopy. *PNAS*, 103:11440–11445, 2006.

[20] R.E. Thompson, D.L. Larson and W.W. Webb. Precise nanometer localization analysis for individual fluorescent probes. *Biophysical Journal*, 82:2775–2783, 2002.

[21] H. Bock, C. Geisler, C.A. Wurm, C. von Middendorff, S. Jakobs, A. Schönle, A. Egner, S.W. Hell and C. Eggeling. Two-color far-field fluorescence nanoscopy based on photoswitchable emitters. *Appl. Phys. B*, 88:161–165, 2007.

[22] S.W. Hell and J. Wichmann. Breaking the diffraction resolution limit by stimulated emission: stimulated-emission-depletion fluorescence microscopy. *Optics Letters*, 19:780ff, 1994.

[23] T.A. Klar and S.W. Hell. Subdiffraction resolution in far-field fluorescence microscopy. *Optics Letters*, 24:954f, 1999.

[24] Thomas A. Klar. *Progress in stimulated emission depletion microscopy*. PhD thesis, Ruperto-Carola University of Heidelberg, 2001.

[25] Jan Keller. *Optimal de-excitation pattern for RESOLFT-microscopy*. PhD thesis, Ruperto-Carola University of Heidelberg, 2006.

[26] S.W. Hell. Strategy for far-field optical imaging and writing without diffraction limit. *Physics Letters A*, 326:140–145, 2004.

[27] S. Inoue. *Handbook of biological confocal microscopy*, pages 1–18. 1995.

[28] V. Westphal, J. Seeger, T. Salditt and S.W. Hell. Stimulated emission depletion microscopy on lithographic nanostructures. *Journal of Physics B*, 38:675–705, 2005.

[29] T.A. Klar, S. Jakobs, M. Dyba, A. Egner and S.W. Hell. Fluorescence microscopy with diffraction resolution barrier broken by stimulated emission. *PNAS*, 97:8206–8210, 2000.

[30] M. Dyba and S.W. Hell. Focal spots of size $\lambda/23$ open up far-field flourescence microscopy at 33nm axial resolution. *Phys. Rev. Lett.*, 88:163910–1ff, 2002.

[31] J. Keller, A. Schönle and S.W. Hell. Efficient fluorescence inhibition patterns for RESOLFT microscopy. *Optics Express*, 15:3361ff, 2007.

[32] V. Westphal and S.W. Hell. Nanoscale resolution in the focal plane of an optical microscope. *Phys. Rev. Lett.*, 94:143903, 2005.

[33] K.I. Willig, S.O. Rizzoli, V. Westphal, R. Jahn and S.W. Hell. STED microscopy reveals that synaptotagmin remains clusted after synaptic vesicle exocytosis. *Nature*, 440:935ff, 2006.

[34] B.H. Soffer and B.B. MacFarland. Continuously tunable, narrow-band organic dye lasers. *Appl. Phys. Lett.*, 10:266f, 1967.

[35] O.G. Peterson, J.P. Webb, W.C. Mccolgin and J.H. Ebely. Organic dye laser threshold. *J. Appl. Phys.*, 42:1917ff, 1971.

[36] J. Widengren and R. Rigler. Mechanisms of photobleaching investigated by fluorescence correlation spectroscopy. *Bioimaging*, 4:149–157, 1996.

[37] Lars Kastrup. *Fluorescence depletion by stimulated emission in single-molecule spectroscopy*. PhD thesis, Ruperto-Carola University of Heidelberg, 2004.

[38] Katrin Willig. *STED microscopy in the visible range*. PhD thesis, Ruperto-Carola University of Heidelberg, 2006.

[39] CERAC Inc. www.cerac.com/pubs/prodata/mgf2.html.

[40] G.N. Lewis and M. Kasha. Phosphorescence and the triplet state. *Journal of the American Chemical Society*, 66:2100–2116, 1944.

[41] C. Ringemann, A. Schönle, A. Giske, C. von Middendorff, S.W. Hell and C. Eggeling. Enhancing fluorescence brightness – effect of reverse intersystem crossing studied by fluorescence fluctuation spectroscopy. *ChemPhysChem*, submitted.

[42] Beat Meyer. *Low temperature spectroscopy*, page 62ff. American Elsevier Publishing Company, Inc., New York, 1971.

[43] A.D. McNaught and A. Wilkinson. *IUPAC compendium of chemical terminology*. International Union of Pure and Applied Chemistry, 2^{nd} edition, 1997.

[44] R. Zondervan, F. Kulzer, S.B. Orlinksii and M. Orrit. Photoblinking of Rhodamine6G in poly(vinyl alcohol): radical dark state formed through the triplet. *J. Phys. Chem. A*, 107:6770–6776, 2003.

[45] Egbert K. Engel. STED-Microscopy mit lateraler Auflösung jenseits der Abbeschen Beugungsgrenze in der Fokalebene, 2001.

[46] H. T. Meryman. Physical limitations of the rapid freezing methods. *Proceedings of the Royal Society of London, Series B*, 147:452–459, 1957.

[47] A. Giske, C. Eggeling and S.W. Hell. Verfahren und Vorrichtung zum räumlich hoch aufgelösten Abbilden einer mit einem Fluoreszenzfarbstoff markierten Struktur. Patentanmeldung: DE 10 2006 011 176.1-52, 2006.

[48] C. Gerthsen und H. Vogel. *Physik, Ein Lehrbuch zum Gebrauch neben Vorlesungen*, page 207f. Springer-Verlag, Berlin, Heidelberg, New York, 17 edition, 1993.

[49] L. Kastrup, H. Blom, C. Eggeling and S.W. Hell. Fluorescence fluctuation spectroscopy in subdiffraction focal volumes. *Phys. Rev. Lett.*, 94:178104, 2005.

[50] M. Dyba and S.W. Hell. Photostability of a fluorescent marker under pulsed excited-stat depletion through stimulated emission. *Appl. Optics*, 42:5123–5129, 2003.

[51] G. Donnert, C. Eggeling and S.W. Hell. Major signal increase in fluorescence microscopy through dark state relaxation. *Nature Methods*, 4:81–86, 2007.

[52] S.M. Mansfielf and G.S. Kino. Solid immersion microscopy. *Appl. Phys. Lett.*, 57:2615–2616, 1990.

[53] Q. Wu, G.D. Feke and R.D. Grober. Realization of numerical aperture 2,0 using a gallium phosphide solid immersion lens. *Appl. Phys. Lett.*, 75:4064–4066, 1999.

[54] M. Hofmann, C. Eggeling, S. Jakobs and S.W. Hell. Breaking the diffraction barrier in fluorescence microscopy at low light intensities by using reversibly photoswitchable proteins. *PNAS*, 102:17565–17569, 2005.

[55] Jan Keller. private communication.